Inter-laboratory Characterisation of Apatite Reference Materials for Oxygen Isotope Analysis and Associated Methodological Considerations

Alicja **Wudarska** (1, 2)* (iD), Michael **Wiedenbeck** (1), Ewa **Słaby** (2) (iD), Małgorzata **Lempart-Drozd** (3), Chris **Harris** (4), Michael M. **Joachimski** (5), Christophe **Lécuyer** (6) (iD), Kenneth G. **MacLeod** (7), Andreas **Pack** (8), Torsten **Vennemann** (9), Frédéric **Couffignal** (1), Dingsu **Feng** (8), Johannes **Glodny** (1), Christof **Kusebauch** (1), Sathish **Mayanna** (1, 10), Alexander **Rocholl** (1), Laura **Speir** (7), Yadong **Sun** (5) and Franziska D. H. **Wilke** (1)

(1) GFZ German Research Centre for Geosciences, Telegrafenberg, Potsdam 14473, Germany
(2) Institute of Geological Sciences, Polish Academy of Sciences, Research Centre in Warsaw, Twarda 51/55, Warsaw 00-818, Poland
(3) Institute of Geological Sciences, Polish Academy of Sciences, Research Centre in Cracow, Senacka 1, Cracow 31-002, Poland
(4) Department of Geological Sciences, University of Cape Town, Rondebosch 7701, South Africa
(5) GeoZentrum Nordbayern, Friedrich-Alexander Universität Erlangen-Nürnberg (FAU), Schlossgarten 5, Erlangen 91054, Germany
(6) Laboratoire de Géologie de Lyon, CNRS UMR 5276, Université Claude Bernard Lyon 1, 2 rue Raphaël Dubois, Villeurbanne 69622, France
(7) Department of Geological Sciences, University of Missouri, Columbia, MO, 65211, USA
(8) Georg-August Universität, Geowissenschaftliches Zentrum, Goldschmidtstrasse 1, Göttingen 37083, Germany
(9) Institute of Earth Surface Dynamics, University of Lausanne, Lausanne CH-1015, Switzerland
(10) Present address: Carl Zeiss Microscopy GmbH, Carl Zeiss Straße 22, Oberkochen 73447, Germany
* Corresponding author. e-mail: ndgiera@cyf-kr.edu.pl

Here we report on the oxygen isotope compositions of four proposed apatite reference materials (chlorapatite MGMH#133648 and fluorapatite specimens MGMH#128441A, MZ-TH and ES-MM). The samples were initially screened for $^{18}O/^{16}O$ homogeneity using secondary ion mass spectrometry (SIMS) followed by $\delta^{18}O$ determinations in six gas source isotope ratio mass spectrometry laboratories (GS-IRMS) using a variety of analytical protocols for determining either phosphate-bonded or "bulk" oxygen compositions. We also report preliminary $\delta^{17}O$ and $\Delta'^{17}O$ data, major and trace element compositions collected using EPMA, as well as CO_3^{2-} and OH^- contents in the apatite structure assessed using thermogravimetric analysis and infrared spectroscopy. The repeatability of our SIMS measurements was better than $\pm$ 0.25 ‰ (1s) for all four materials that cover a wide range of $10^3\delta^{18}O$ values between +5.8 and +21.7. The GS-IRMS results show, however, a significant offset of $10^3\delta^{18}O$ values between the "phosphate" and "bulk" analyses that could not be correlated with chemical characteristics of the studied samples. Therefore, we provide two sets of working values specific to these two classes of analytical methodologies as well as current working values for SIMS data calibration.

Keywords: secondary ion mass spectrometry, TC/EA, laser fluorination, thermogravimetry, infrared spectroscopy.

Since the 1950s, oxygen isotope compositions of minerals of the apatite group have been considered valuable archives for reconstructing palaeoenvironmental conditions (Urey *et al.* 1951). In particular, $^{18}O/^{16}O$ ratios of biologically produced hydroxylapatite $Ca_{10}(PO_4)_6(OH)_2$ and fluorapatite $Ca_{10}(PO_4)_6F_2$ – the main components of bones, teeth, and of some microfossils such as conodonts – have been found useful in palaeoclimate studies (e.g.,

Longinelli 1965, Kolodny *et al.* 1983, Longinelli 1984, Luz *et al.* 1984, Luz and Kolodny 1985, Kohn and Cerling 2002). Although research on oxygen isotope compositions has mostly focused on bioapatite, applications of this isotopic system to other geological materials have also been explored (e.g., phosphorite and igneous rocks, Shemesh *et al.* 1983, Decrée *et al.* 2020). In the work by Blake *et al.* (2010), oxygen isotope compositions of phosphates in

metasedimentary rocks were used to distinguish samples affected by secondary veining from those recording biological processing in equilibrium with ocean waters, while Bruand *et al.* (2019) showed that oxygen isotopes in apatite may be a useful source of information about crustal evolution. Oxygen isotope ratios have been routinely used as a tracer for sources and cycling of phosphate in aquatic and soil environments (e.g., McLaughlin *et al.* 2006, Jaisi and Blake 2014, Xu *et al.* 2018). The $^{18}O/^{16}O$ ratio has also been proposed as a potential biomarker for life on Mars (Greenwood *et al.* 2003). Furthermore, with improvements in analytical techniques, it has become possible to expand the utility of $^{18}O/^{16}O$ studies with measurements of $^{17}O/^{16}O$ ratios (e.g., Miller and Pack 2021, Passey and Levin 2021). Oxygen triple-isotope applications include, among others, identification of diagenetic changes in the skeletal apatite of small mammals (Gehler *et al.* 2011) and a study of hydrosphere–lithosphere interactions on Mars (Bellucci *et al.* 2020).

According to the IUPAC Technical Report (Brand *et al.* 2014) and following further recommendations for isotope data presentation by Coplen (2011), the ratio of the two stable oxygen isotopes ^{18}O and ^{16}O in a sample should be expressed in relation to Vienna Standard Mean Ocean Water (VSMOW, $^{18}O/^{16}O = 2005.20 \pm 0.45 \times 10^{-6}$, Baertschi 1976) using the equation:

$$\delta^{18}O = \frac{^{18}O/^{16}O_{sample}}{^{18}O/^{16}O_{VSMOW}} - 1 \qquad (1)$$

Furthermore, it has been recommended to report the relative difference of isotope ratios as $10^3\delta^{18}O$, rather than in commonly used per mil (‰) notation (Coplen 2011, Meisel 2019). In this contribution, however, we continue to use ‰ notation to both express measurement repeatability, which was calculated as relative standard deviation, and to report the difference in instrumental mass fractionation (IMF) in SIMS analyses. Additionally, when quantifying the actual divergence of the measured isotope ratios from the true values defined by gas source isotope ratio mass spectrometry (GS-IRMS), we applied the widely used notation:

$$\alpha_{inst} = (^{18}O/^{16}O)_{meas}/(^{18}O/^{16}O)_{true} \qquad (2)$$

which is a dimensionless value directly related to the IMF-induced bias according to:

$$IMF = (\alpha_{inst} - 1) \times 1000 \qquad (3)$$

The value $\delta^{17}O$ is defined analogously to $\delta^{18}O$:

$$\delta^{17}O = \frac{^{17}O/^{16}O_{sample}}{^{17}O/^{16}O_{VSMOW}} - 1 \qquad (4)$$

where $^{17}O/^{16}O_{VSMOW} = 379.9 \pm 0.8 \times 10^{-6}$ (Li *et al.* 1988). Small deviations from the mass-dependent reference line between $\delta^{18}O$ and $\delta^{17}O$ are expressed in the form of the $\Delta'^{17}O$ notation (Miller *et al.* 2020):

$$\Delta'^{17}O = \ln(\delta^{17}O + 1) - \lambda_{RL}\ln(\delta^{18}O + 1) \qquad (5)$$

The choice of the "correct" reference line slope (λ_{RL}) is still a matter of debate. Pack and Herwartz (2014) used a slope of 0.5305, which is the high-*T* approximation for oxygen isotope equilibrium fractionation. The researchers working with water samples have chosen a value of 0.528, which is the slope defined by the two reference samples VSMOW and SLAP (Standard Light Antarctic Precipitation; Schoenemann *et al.* 2013). Sharp *et al.* (2018) favoured a reference line slope of 0.528 also for rocks and minerals to get the "rock and water communities" on the same scales with respect to $\Delta'^{17}O$. Here, we adopt $\lambda_{RL} = 0.528$ for the definition of $\Delta'^{17}O$. Currently, there is no characterised reference material available for $\Delta'^{17}O$ measurements.

Most existing research devoted to the oxygen isotope composition of bioapatite has been conducted using GS-IRMS. Depending on the actual sample preparation protocol used, data for either a specific component (PO_4^{3-}, CO_3^{2-}) or for the "bulk" oxygen within an apatite sample can be determined (e.g., Crowson *et al.* 1991, O'Neil *et al.* 1994, Vennemann *et al.* 2002, Lécuyer 2004). It is to be noted here that we define the term "bulk" to specify all oxygen atoms contained in a given material regardless of their locations within the crystal lattice. Oxygen isotopic studies can also be performed using secondary ion mass spectrometry (e.g., Eiler *et al.* 1997), which enables *in situ* analysis using < 20 μm spot size diameter and, therefore, can be exceptionally useful for measurements of heterogeneous samples or in those cases where only limited amounts of research material are available (e.g., extraterrestrial samples and unique fossils). The main limitation of SIMS is the fact that it requires homogeneous, well-characterised, and matrix-matched reference materials (RMs). Durango fluorapatite (Cerro de Mercado, Mexico) is the most commonly used RM for calibrating $\delta^{18}O$ SIMS analyses of apatite (Trotter *et al.* 2008, 2015, Wheeley *et al.* 2012, Žigaitė and Whitehouse 2014, Xu *et al.* 2015, Chen *et al.* 2016, 2020, Zeng *et al.* 2016, Bruand *et al.* 2019, Bellucci *et al.* 2020, Yang *et al.* 2020, Edwards *et al.* 2022, Zhang *et al.* 2021). However, the study by Sun *et al.* (2016) showed that not every Durango specimen is homogeneous and reported an inter-crystal $10^3\delta^{18}O$ range of 4.4. Therefore,

Durango may not be suitable for calibration of $\delta^{18}O$ measurements by SIMS. Yang *et al.* (2020) tested a number of apatite samples using SIMS and selected potential RMs candidates for oxygen isotopic measurement. These authors, however, did not provide any GS-IRMS data, which is a crucial step for characterisation in advance of using a material for SIMS data calibration. In contrast, Li *et al.* (2021) reported both SIMS and GS-IRMS datasets for the Qinghu-AP reference material along with further guidelines on potential artificial effects that may influence *in situ* $\delta^{18}O$ measurements. That study, however, did not take inter-laboratory bias into account, providing GS-IRMS data from only one laboratory.

Primarily in support of the SIMS community, we undertook this study to characterise both the chemical and oxygen isotope compositions of a new suite of potential apatite RMs. Previous isotopic research on phosphate materials has shown that different analytical techniques often yield differing $\delta^{18}O$ values (e.g., Lécuyer *et al.* 1993, Vennemann *et al.* 2002, Pucéat *et al.* 2010). Inter-laboratory bias, which results from differences in analytical protocols, has also been reported for other isotopic systems and materials (e.g., Gonfiantini *et al.* 2003, MacLeod 2012, Manzini *et al.* 2017, Wiedenbeck *et al.* 2021, Wudarska *et al.* 2021). Therefore, in order to establish the extent of inter-laboratory bias for oxygen isotope analysis of apatite, we measured $\delta^{18}O$ values at six GS-IRMS laboratories, applying a variety of sample preparation protocols.

Sample selection and description

A total of fifty-eight natural apatite samples provided by mineralogical museums and mineral collectors were tested for oxygen isotope ($\delta^{18}O$) homogeneity using SIMS. A set of four specimens (Figure 1, Table 1), that both proved to be adequately homogeneous in their $^{18}O/^{16}O$ (repeatability of measurements ≤ 0.25 ‰, $1s$) and that also represented various members of apatite solid solution series $Ca_{10}(PO_4)_6(F, Cl,OH)_2$, were further investigated using SEM-EDS, EPMA, thermogravimetry coupled to quadrupole mass spectrometry (TG-MS), infrared spectroscopy (IR), SIMS, and GS-IRMS. These four materials were cleaned using acetone and distilled water and were crushed and sieved to obtain a grain-size fraction between 63 and 1400 µm; these subsequently underwent mineral separation and were then split using a riffle splitter resulting in multiple units (Table 1). Mineral separation procedures were tailored to each sample individually depending on the amounts and types of non-apatite material that was present in these samples.

MGMH#133648 consists of six yellow-white crystals of chlorapatite from Norway, of which only one fragment

(~ 11.4 g, shown in Figure 1) was selected for this study. The same material was part of an earlier study of apatite RMs for chlorine isotope analysis (Wudarska *et al.* 2021). The remaining material (~ 13.2 g) was returned to the Mineralogical and Geological Museum at Harvard University. A white crust of hydroxylapatite was removed from the surface of the chlorapatite crystal using a circular saw and a micro-drill grinding tool. The crushed material underwent magnetic (Frantz magnetic separator) and density separation (using bromoform as a heavy liquid with 2.84 g cm^{-3} density). MGMH#133648 contains minor amounts of inclusions of hydroxylapatite, Ca-Mg-Fe-silicates and aluminosilicates, and calcite.

MGMH#128441A is a yellow-coloured crystal of fluorapatite, which was selected for both this study and earlier work on apatite RMs for chlorine isotope analysis (Wudarska *et al.* 2021) from eight specimens from Colorado, USA; the other seven specimens were returned to the Mineralogical and Geological Museum at Harvard University. A dark green-coloured mineral (possibly amphibole) was removed from the surface and from a cavity inside of the selected crystal using a micro-drill. The crushed material underwent magnetic (Frantz) separation. MGMH#128441A contains minor amounts of inclusions of Fe-oxides, Ca-Mg-Fe-Mn silicates and aluminosilicates, and monazite. This apatite specimen shows a resemblance to the fluor-chlor-oxy apatite from the Crystal Lode pegmatite near Eagle, Colorado (Young and Munson 1966), having greenish-yellow colours and very similar chemical characteristics.

MZ-TH is a greenish-yellow crystal of fluorapatite from Tory Hill, Ontario, Canada. The crushed material was soaked in an acidic, sugar-free cola beverage (pH = 2, containing phosphoric acid with a molar concentration of ~ 4 mmol l^{-1}) in an ultrasonic bath for ~ 5 h, which successfully removed most of the iron oxide staining from the crystal surface. The sample was then cleaned in acetone and distilled water and underwent magnetic (Frantz) separation. MZ-TH contains minor amounts of non-apatite impurities, such as iron oxides and Fe-Mg aluminosilicates.

ES-MM is a blue-coloured, gem-quality fluorapatite crystal from Le U Village, Mogok, Myanmar. Prior to crushing, the crystal surface was cleaned using a micro-drill in order to remove traces of glue, which had been used for mounting the crystal for exhibition purposes by a mineral dealer. The sample did not require mineral separation, but trace amounts of rounded inclusions were observed in polished crystal fragments: K-Na-aluminosilicates (some of which containing Cl), quartz, and Mg-Na-K-silicate. The ES-MM apatite shows a resemblance to the MK-1 specimen

Figure 1. Photographs of the unprocessed apatite samples characterised in this study. Total masses of crushed apatite material produced after completion of mineral separation are given in the bottom left of each panel. The two specimens MGMH#133648 and MGMH#128441A have already been characterised for their chlorine isotope compositions by Wudarska *et al.* (2021).

described by Wu *et al.* (2019) as a new potential reference material for (U-Th)/He dating. Both ES-MM and MK-1 are gem-quality crystals sampled in the area of Mogok, Myanmar. However, due to the fact that ES-MM was purchased from a mineral dealer, its exact sampling location and the relationship to MK-1 crystal are unknown.

Both the Durango apatite (Mexico, sample details in Wudarska *et al.* 2021) and NIST SRM 610 glass served as test samples and quality control (QC) materials for SIMS analyses in this study. SARM 32, which is a reference material derived from an industrial by-product of copper ore flotation, and which consists of fluorapatite (igneous in origin) with an admixture of dolomite and calcite as well as trace amounts of phlogopite and vermiculite, was used as a fine-grained material for $\delta^{18}O$ determinations in multiple GS-IRMS laboratories meant for evaluating inter-laboratory bias. The material has been widely used as a phosphate RM for XRF analysis. Additionally, tooth enamel of a modern African elephant (AG-LOX) was tested to assess inter-laboratory bias for oxygen isotope measurements of biogenic apatite. This material has previously been used as an internal reference sample for $\delta^{18}O$ and $\delta^{13}C$

measurements of the carbonate component in apatite (Gehler *et al.* 2012).

Analytical methods

Sample preparation

The measurements of $\delta^{18}O$ values in the GS-IRMS laboratories conducting analyses of phosphate-bonded oxygen were performed on identical ~ 0.1 g units obtained from the splitting process described above. In contrast, $\delta^{18}O$ and $\delta^{17}O$ determinations in the GS-IRMS laboratories conducting "bulk" measurements, as well as the TG and IR determinations of CO_3^{2-} and OH^- contents in the apatite structure were performed on the apatite crystals that were carefully hand-picked from the produced splits beforehand in order to eliminate non-apatite inclusions and coatings.

For EPMA and SIMS analyses, the apatite crystals were mounted in the centre of 25.4-mm (1 inch) diameter acrylic discs using Epofix cold-setting epoxy resin, which were subsequently polished to a < 5 μm surface quality. A total of five mounts were produced:

Table 1.
List of the apatite samples and other materials used in this study

Sample ID	Type	Source	Origin	Total mass (g)[a]	Number of splits
MGMH#133648	chlorapatite	Mineralogical and Geological Museum at Harvard University	Norway, unknown locality	9.2	128
MGMH#128441A	fluorapatite	Mineralogical and Geological Museum at Harvard University	Colorado, USA	84.0	512
MZ-TH	fluorapatite	Michael Zolensky	Tory Hill, Ontario, Canada	38.4	512
ES-MM	fluorapatite	Mineral dealer	Le U Village, Mogok, Myanmar	4.2	32
TUBAF#43[b]	fluorapatite	TU Bergakademie Freiberg	Eganville, Renfrew, Ontario, Canada	90.3	512
Dur	fluorapatite	Mineral dealer	Durango, Cerro de Mercado, Mexico	---	---
NIST SRM 610	synthetic glass	National Institute of Standards and Technology, USA		---	---
SARM 32	phosphate beneficiation product of flotation tailings	South African Reference Material, Phalaborwa, Limpopo Province		---	---
AG-LOX	biogenic apatite	Tooth enamel of a modern African elephant		---	---

[a] Total masses of crushed apatite material produced after completion of mineral separation, which was subsequently split into metrologically identical units.
[b] TUBAF#43 was ultimately not selected for a detailed investigation by IR, TG, and GS-IRMS. The sample description and the data collected using SEM-EDS, EPMA, and SIMS are included in Appendix S1 for future reference.

● Mount #1, Mount #2, and Mount #3: multiple random crystals of MGMH#133648, MGMH#128441A, MZ-TH, and ES-MM, which were obtained from the splitting process described above, mounted with fragments of both Durango apatite and NIST SRM 610 glass (Figure 2);

● Mount #4: a portion of the white crust of hydroxylapatite mechanically removed from the surface of the MGMH#133648 sample (see section "*Sample selection and description*") was embedded in epoxy to assess its isotopic composition. This examination was performed in order to investigate the minor amounts of this crust that we were unable to fully eliminate prior to sample splitting (see Appendix S2 and Wudarska *et al.* 2021);

● Mount #5: three fragments of the Durango single crystal, which represent different orientations with respect to the crystallographic *c*-axis (Appendix S3 and also Wudarska *et al.* 2021).

SEM-EDS and FE-SEM-EBSD analyses

The major element chemical compositions of the phases associated with our four apatite test samples were determined at the Helmholtz Centre Potsdam (GFZ) using a Carl Zeiss Ultra Plus field emission scanning electron microscope equipped with an EDS detector (Thermo Fisher Scientific), which was operated at 20 kV accelerating voltage.

Additionally, the crystal orientations of the Durango apatite fragments selected for assessing the influence of crystallographic orientation effects on SIMS-determined $^{18}O/^{16}O$ ratios were established using the electron backscatter diffraction technique (EBSD). EBSD point analyses and mapping (at 0.2 μm step size) were performed using a FEI Quanta 3D field emission scanning electron microscope equipped with an EBSD detector (EDAX). For details concerning EBSD analyses, see Wudarska *et al.* (2021).

EPMA chemical analyses

Quantitative chemical analyses of apatite crystals were performed using the JEOL Hyperprobe JXA-8500F microprobe at the GFZ. Details of the analytical protocol as well as the spectral lines, corresponding peak counting times, and the calibration materials are presented in Wudarska *et al.* (2021). Briefly, the samples were coated with a 20-nm thick carbon film and analysed for major and trace elements using an acceleration voltage of 15 kV, a spot size of 10 μm, and two different beam current settings: 5 nA and 40 nA, respectively. Very low electron beam current of 5 nA and relatively large beam diameter were applied in order to suppress possible volatile (F and Cl) diffusion (e.g., Stormer *et al.* 1993, Goldoff *et al.* 2012), while high-electron beam current of 40 nA was used to detect REE and other trace elements. Calculations of the apatite formulae based on the data acquired with 5 nA were performed using the method
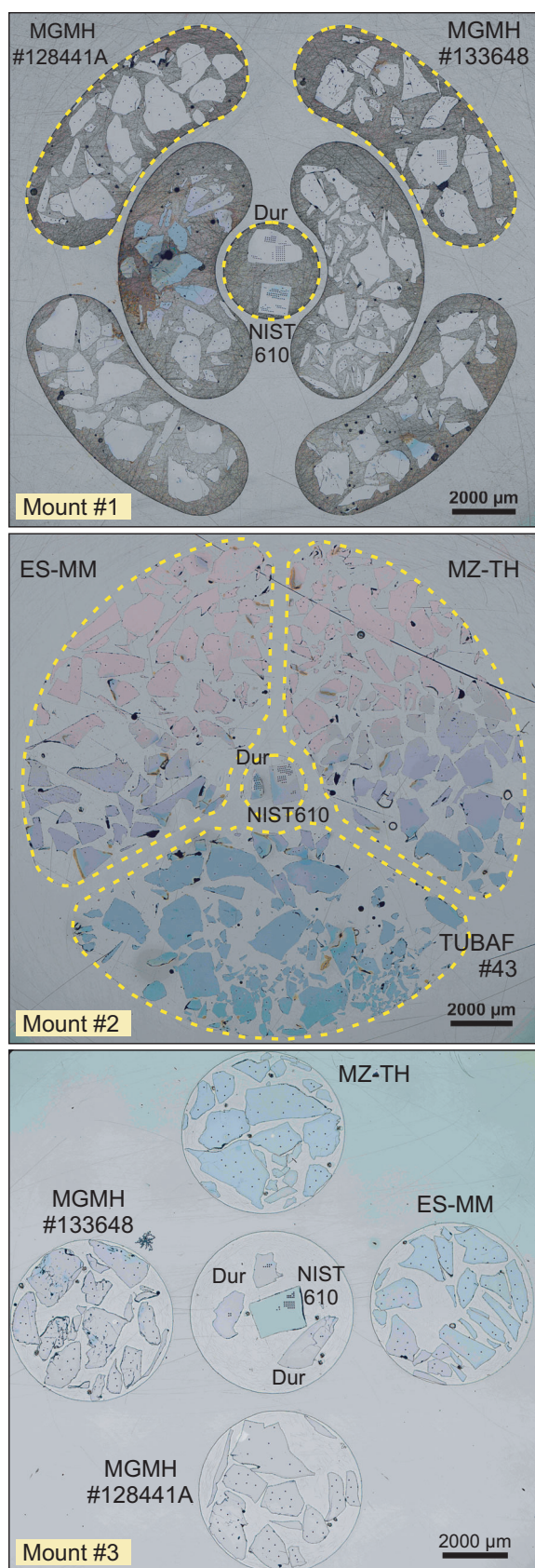
Figure 2. Reflected-light optical images of three gold-coated SIMS mounts. The photographs were taken after SIMS $\delta^{18}O$ measurements, such that they show the distribution of the analytical spots (black). Mount #1 has previously been used for a chlorine isotope study (Wudarska *et al.* 2021), and therefore, the analytical spots from $\delta^{37}Cl$ measurements are also visible in the upper part of the figure. NIST SRM 610 silicate glass and Durango apatite (Dur) were used for tuning purposes and instrumental drift assessment.

of Ketcham (2015) with a normalisation procedure based on twenty-five oxygen equivalents.

Assessment of CO_3^{2-} and OH^- content in the apatite structure by thermogravimetry with evolving gas analysis and infrared spectroscopy

Those apatite crystals that had been hand-picked for thermogravimetry coupled with quadrupole mass spectrometry and infrared spectroscopy experiments were gently ground in an agate mortar followed by analysis in the Clay Minerals Laboratory at the Institute of Geological Sciences of the Polish Academy of Sciences in Cracow. A thermogravimetric TA Discovery (TA Instruments, USA) analyser with a weighing uncertainty of < 1 μg, mass measurement accuracy of < 0.1 μg, and a thermal drift between 200 °C and 1000 °C of < 4 μg was used for heating experiments. For evolved gas analysis, the TG analyser was coupled to a ThermoStar^{TM}, GDS 320 quadrupole mass spectrometer (Pfeiffer Vacuum, Germany) using an electron impact ionisation energy of 70 eV. An amount of 21 mg of each powder sample was loaded into a Pt crucible and heated under fast heating condition with a 20°C min^{-1} ramp rate up to 1000 °C in dry nitrogen atmosphere ($> 99.999\%$ purity) with a flow rate of 100 cm^3 min^{-1}. The fast ramp heating condition was necessary in order to collect a measurable portion of the evolved gas for a sufficient MS signal as a function of time and temperature. The total mass loss (Δm_{total}) on TG curves was calculated as the difference between the mass at 105 °C and the minimum mass determined at 1000 °C. The following molecules expected to be evolved from samples during heating were monitored: H_2O^+ $m/z = 18$, CO_2^+ $m/z = 44$, CO^+ $m/z = 28$, SO_2^+ $m/z = 64$, NH_3^+ $m/z = 17$, and their daughter ions. The MS dwell time was 200 ms; thus, one scan was collected every 2 s for the selected molecules. The background contributions of MS measurements were based on blank (empty TG pan) measurements. The measured mass spectra are presented here without background correction.

Infrared spectra were collected using a Nicolet 6700 spectrometer with a DTGS KBr detector (Thermo Scientific, Waltham, Massachusetts, USA), using a diffuse reflection (DRIFT) technique with Praying Mantis (Harrick, USA) accessory. A 1-mg portion of each powder sample was mixed and ground with 200 mg of KBr. Spectra were collected over 4000–450 cm^{-1} range at a resolution of 4 cm^{-1} with 128 scans averaged. The absorbance maxima were determined from the second-derivative minima (Savitzky–Golay, thirteen point-smoothing) using the OMNIC software package (Thermo Fisher Scientific). IR-DRIFT analyses were conducted for both the natural raw apatite samples and the residues from the thermogravimetric experiments (the final products of sample heating to 1000 °C).

For result comparison, additional IR measurements in the Attenuated Total Reflection (ATR) technique were performed for both the natural raw apatite samples and the heating products. All IR and TG-MS measurements were repeated at least twice to check the reproducibility of the results.

SIMS oxygen isotope ratio homogeneity test

In situ measurements of $^{18}O/^{16}O$ ratios were conducted using the Cameca 1280-HR large geometry SIMS instrument at the GFZ. Prior to analyses, the sample mounts were cleaned in high-purity ethanol and were then coated with a 35-nm thick, high-purity gold film to ensure electrical conductivity. A nominally 2 nA, 10 keV $^{133}Cs^+$ primary ion beam was used to produce $^{18}O^-$ and $^{16}O^-$ secondary ions. Using a 25 μm × 25 μm raster, the sample surface was sputtered for 70 s to remove the gold coating to suppress surface contaminants and to establish equilibrium sputtering conditions. The raster was then reduced to a 15 μm × 15 μm area, from which $^{18}O^-$ and $^{16}O^-$ secondary ions were collected simultaneously on two Faraday cups over twenty cycles with each cycle lasting for 4 s. The mass resolution of the instrument was $M/\Delta M \approx 2000$ (at 10% peak height).

Multiple analyses ($n = 28$–51) were performed on multiple fragments ($n = 9$–20) of all four apatite samples in Mounts #1, #2, and #3 (Figure 2). The measurements on Mount #1 and Mount #2 were conducted in two fully automatic, chain-analysis sequences in June 2018. These results, though providing the information on homogeneity of the samples, could not be used for inter-comparison of IMF factors between the four samples. Therefore, additional analyses of random fragments embedded in Mount #3 were conducted in September 2020. During both sessions, analytical spots were widely spaced and selected in a quasi-random fashion. Instrumental drift was monitored *via* analyses on both the Durango apatite and NIST SRM 610

glass fragments that were regularly interspersed throughout the run. Additional test of selected fragments of MGMH#133648 embedded in Mount #4 (Appendix S2) and the three crystallographically oriented fragments of the Durango apatite in Mount #5 (Appendix S3) were conducted in November 2019 and February 2020, respectively, following a similar analytical protocol.

A typical count rate for $^{16}O^-$ ions was ~ 2×10^9 cps. The depth of sputtered sample pits was ~ 0.85 μm, and the amount of consumed material during each analysis was ~ 400 pg as based on white light interferometry (for a 3D image of a typical SIMS crater, see Appendix S4).

$\delta^{18}O$ values determination by GS-IRMS

Determination of $\delta^{18}O$ values was conducted independently in six GS-IRMS laboratories applying their own established analytical protocols; these fall into two groups: high-temperature reduction of Ag_3PO_4 (determinations of phosphate-bonded oxygen using high-temperature conversion-elemental analyser, herein after referred to as Ag_3PO_4-TC/EA) and laser fluorination (analyses of "bulk" oxygen, herein after referred to as LF). Additionally, in one of the laboratories using the fluorination method, $\delta^{17}O$ data were also collected. All GS-IRMS measurements were calibrated using a suite of reference materials and quality control samples that are listed in Table 2.

SARM 32 powdered phosphate rock was selected as a direct intercomparison material that was analysed along with the apatite samples in all laboratories. As a widely used phosphate RM for XRF analysis, this material has been shown to be homogeneous in terms of elemental concentrations (Hansen 1985). SARM 32 has also been repeatedly analysed using GS-IRMS at FAU Erlangen-Nürnberg ($n = 150$ over the course of three years, Appendix S5). Furthermore, AG-LOX bioapatite was analysed in two laboratories at the Georg-August Universität, Göttingen, in order to compare the results obtained using both Ag_3PO_4-TC/EA and LF methods. Here, we provide a brief description of the laboratory methods used by the GS-IRMS facilities.

Oxygen isotope analysis of phosphate at FAU Erlangen-Nürnberg: Chemical conversion of apatite-bound phosphate into trisilverphosphate was performed following the methods described by Crowson *et al.* (1991), Lécuyer *et al.* (1993), O'Neil *et al.* (1994), and Joachimski *et al.* (2009). The apatite samples and the phosphate rock SARM 32 were prepared in duplicates: a portion (~ 1 mg) of each sample (previously powdered in an agate mortar) was weighed into small PE beakers and dissolved by adding

Table 2.
List of reference materials and quality control materials used for calibration of GS-IRMS analyses

"Phosphate" $\delta^{18}O$ analyses		Uni Erlangen	Uni Lyon	Uni Missouri
Reference materials	Type of RM and reference $10^3\delta^{18}O_{VSMOW}$ values	TU1 (21.11)[a] TU2 (5.45)[a]	NBS 120c (21.7)[b] NBS127 (9.3)[d] CAL3 (6.0)[e]	a large "batch" of silver phosphate generated from NBS120c (21.7)[b]
	Measured $10^3\delta^{18}O_{VSMOW}$ values $\pm\ 1s$	TU1: 21.10 $\pm$ 0.13 ($n = 6$) TU2: 5.45 $\pm$ 0.02 ($n = 6$)	NBS120c: 21.57 $\pm$ 0.25 ($n = 5$) NBS127: 9.16 $\pm$ 0.17 ($n = 5$) CAL3: 5.85 $\pm$ 0.18 ($n = 5$)	NBS120c: 22.28 $\pm$ 0.34 ($n = 24$)
Quality control materials	Type of QC and reference $10^3\delta^{18}O_{VSMOW}$ values	NBS120c (21.7)[b] Ag₃PO₄ (9.9)[c]	NBS120c (21.7)[b]	NBS120c (21.7)[b] Benzoic acid (~24–25)[f]
	Measured $10^3\delta^{18}O_{VSMOW}$ values $\pm\ 1s$	NBS120c: 21.43 $\pm$ 0.16 ($n = 19$) Ag₃PO₄: 9.87 $\pm$ 0.19 ($n = 13$)	NBS120c: 21.57 $\pm$ 0.25 ($n = 5$)	NBS120c: 21.95 $\pm$ 0.31 ($n = 12$)[g] Benzoic acid: 24.33 $\pm$ 0.08 ($n = 15$)
"Bulk" $\delta^{18}O$ analyses		Uni Cape Town	Uni Göttingen	Uni Lausanne
Reference materials	Type of RM and reference $10^3\delta^{18}O_{VSMOW}$ values	MONGT (5.38)[h]	UWG-2: (5.8)[i] San Carlos (5.12)[i]	NBS-28: (9.64)[k] LS-1 (18.1)[l]
	Measured $10^3\delta^{18}O_{VSMOW}$ values $\pm\ 1s$	MONGT: 5.38 $\pm$ 0.12 ($n = 10$)	UWG-2: 5.80 ($n = 1$) San Carlos: 5.25 ($n = 1$)	NBS-28: 9.19 ($n = 11$)

[a] synthetic Ag₃PO₄ prepared from K₂HPO₄ (Vennemann *et al.* 2002).
[b] SRM120c, Florida Phosphate Rock (Lécuyer *et al.* 1993).
[c] commercial synthetic Ag₃PO₄.
[d] BaSO₄ (Gonfiantini *et al.* 1995).
[e] synthetic in house-made Ag₃PO₄ (Lécuyer *et al.* 2019).
[f] C₇H₆O₂ (quality control material for monitoring the machine performance only).
[g] A portion of NBS120c prepared and measured as an unknown. $10^3\delta^{18}O_{VSMOW}$ values were adjusted to nominal value of 21.7 for the mean of NBS-120c (batch) run on the same day.
[h] Garnet (Harris and Vogeli 2010).
[i] Garnet (Valley *et al.* 1995).
[i] Olivine (Pack *et al.* 2016).
[k] Quartz (Coplen *et al.* 1983).
[l] Quartz (Seitz *et al.* 2017).

5 ml of 2 mol l⁻¹ HNO₃. After neutralising the solutions with 2 mol l⁻¹ KOH, Ca²⁺ was precipitated as CaF₂ by adding 2 mol l⁻¹ HF. The solutions were centrifuged, and the supernatant solutions were transferred to clean beakers. Silver amine solution; containing 0.34 g of AgNO₃, 0.28 g of NH₄NO₃, 1 ml of NH₄OH, and filled with deionized water to a volume of 30 ml; was subsequently added in order to precipitate the phosphate as Ag₃PO₄. The beakers were stored for 8 h in a drying oven at 60 °C. As NH₄⁺ was slowly evolving, the pH of the solution decreased, and Ag₃PO₄ crystals started to precipitate. The Ag₃PO₄ crystals were extensively rinsed with deionized water, dried at 50 °C, and homogenised using a small agate mortar.

The samples and internal reference materials were generally measured in triplicates (except for two dissolutions of MGMH#133648 that were measured six and ten times). For a single analysis, 200–300 µg of Ag₃PO₄ were weighed onto silver foil and transferred to the sample carousel of the TC/EA coupled online to a ThermoFisher Delta V Plus mass spectrometer. The He flow rate was 80 ml s⁻¹, reactor temperature was set to 1450 °C, and the column temperature was 90 °C. At 1450 °C, silver phosphate reacted with glassy carbon in the reactor, and CO formed as the analyte (Vennemann *et al.* 2002). Generated CO was transferred in a helium stream through a gas chromatograph and a Conflo IV interface to the mass spectrometer.

The measurements were calibrated using a two-point calibration (Paul *et al.* 2007) based on the reference samples TU1 ($10^3\delta^{18}O_{VSMOW} = +21.11$) and TU2 ($10^3\delta^{18}O_{VSMOW} = +5.45$, Vennemann *et al.* 2002). Two quality control samples – NBS120c ($10^3\delta^{18}O_{VSMOW} = +21.7$, Lécuyer *et al.* 1993) and a commercial Ag₃PO₄ ($10^3\delta^{18}O_{VSMOW} = +9.9$) – were prepared along with the apatite samples and measured as unknowns.

Oxygen isotope analysis of phosphate at the Université Claude Bernard Lyon 1: The apatite samples were ground to grain size ~ 100 μm. After dissolution of powdered apatite samples and SARM 32 (~ 5 mg each) in 2 mol l^{-1} of HF at 25 °C for 24 h, the CaF$_2$ that precipitated was separated from the solution by centrifugation. The CaF$_2$ precipitate was rinsed three times using double-distilled water, and the rinse water was added to the solution, which was subsequently neutralised with a 2 mol l^{-1} KOH. Cleaned Amberjet strong anion exchange resin (2 ml) was added to the neutralised solution in polypropylene tubes. The tubes were placed on a shaker table for 12 h to promote the ion exchange process. Excess solution was discarded, and the resin was washed five times with double distilled water to remove the traces of ionic contaminants. To elute the phosphate ions quantitatively from the resin, 25–30 ml of 0.5 mol l^{-1} NH$_4$NO$_3$ was added to adjust the pH of the solution to between 7.5 and 8.5, and the tubes were then gently shaken for about 5 h. The solution was placed in a 250-ml Erlenmeyer flask and *circa* 1 ml of concentrated NH$_4$OH was added to raise the pH to 9–10. Fifteen millilitres of ammoniacal AgNO$_3$ solution was added to the flask. Upon heating this solution to 70 °C in a thermostatic bath, millimetre-sized yellow crystals of Ag$_3$PO$_4$ precipitated. The crystals of silver phosphate were collected on a Millipore filter, washed three times with double-distilled water, and air-dried at 50 °C.

Approximately 500 μg of the silver phosphate sample were mixed with 500 μg of carbon black powder and loaded in silver foil capsules. Pyrolysis was performed at 1450 °C with a glassy carbon reactor using a varioPYR-Ocube^{TM} Elemental Analyser interfaced in the Continuous-Flow mode with an Isoprime^{TM} Isotopic Ratio Mass Spectrometer.

The measurements were calibrated by performing a three-point calibration using the reference samples NBS120c (10$^3\delta^{18}$O$_{VSMOW}$ = +21.7, Lécuyer *et al.* 1993), NBS127 (BaSO$_4$, 10$^3\delta^{18}$O$_{VSMOW}$ = +9.34, Gonfiantini *et al.* 1995), and CAL3 (an internal reference of synthetic homemade Ag$_3$PO$_4$; 10$^3\delta^{18}$O$_{VSMOW}$ = +6.0, Lécuyer *et al.* 2019).

Oxygen isotope analysis of phosphate at the University of Missouri: δ^{18}O values were measured following the method described by Quinton and MacLeod (2014). The apatite samples and SARM 32 were soaked in ~ 5% NaOCl for 4–24 h and then rinsed three to five times with double-distilled water and dried at < 50 °C. The samples were prepared in four or five replicates: a portion (0.9–2.2 mg) of each sample was dissolved in 100 ml of

0.5 mol l^{-1} HNO$_3$. The solutions were centrifuged, and the supernatant solutions were transferred to the cation exchange column. Cations were bound to the resin, while phosphate was eluted with 1 ml of double-distilled water. The eluant was collected in 2-ml centrifuge tubes to which 150 ml of 2 mol l^{-1} NH$_4$OH, and 150 ml of silver amine solution (0.4 mol l^{-1} of AgNO$_3$ and 0.7 mol l^{-1} of NH$_4$NO$_3$) was added and then swirled with a vortex mixer. The vials were placed, with lids open, in a 50-°C drying oven overnight. Crystallisation of Ag$_3$PO$_4$ occurred as NH$_4^+$ escaped from the solution and pH dropped. Ag$_3$PO$_4$ crystals were then rinsed with double de-ionised water three to four times and dried at 50 °C.

For each analysis, approximately 500 μg of Ag$_3$PO$_4$ was weighed and packed in 3.5 mm × 5 mm pressed silver capsules and loaded into the autosampler of a Thermo-Finnigan TC/EA. The samples were then dropped into a graphite crucible within a glassy carbon tube filled with glassy carbon chips. Pyrolysis was achieved at 1400 °C, resulting in the reduction of Ag$_3$PO$_4$. The liberated oxygen then reacted with the glassy carbon to form CO gas (Vennemann *et al.* 2002). The resultant CO gas was transferred by He stream through a gas chromatograph held at 90 °C and analysed online using a continuous-flow Thermo-Finnigan Delta Plus XL gas source mass spectrometer.

The measurements were calibrated using a large "batch" of silver phosphate generated from NBS120c (10$^3\delta^{18}$O$_{VSMOW}$ = +21.7, Lécuyer *et al.* 1993). Additionally, the NBS120c sample was prepared along with the apatite samples and measured as an unknown. The CO yield and the mass spectrometer performance were monitored using benzoic acid (10$^3\delta^{18}$O$_{VSMOW}$ = ~ 24–25) as a quality control sample, which was analysed three to four times each day (Table 2).

Each individual dissolution (*n* = 4 or 5) produced from the apatite samples and SARM 32 was analysed two to eight times (a total of 11–23 aliquots per sample). The analytical precision of 10$^3\delta^{18}$O determinations was usually better than ± 0.3 (1 standard deviation). When a replicate differed from the mean 10$^3\delta^{18}$O value for that sample by > ± 0.6 (i.e., 2 standard deviations), the outlier was removed from consideration, and a new sample mean was calculated for use in plotting and interpretation. This screening test flagged as suspect eight out of a total eighty-two analyses (1–3 per sample). Although excluded from plots, these outliers are still listed in the data tables. Possible explanations for anomalous measurements are contamination by other oxygen-bearing phases (traces of nitrate or organic matter) or instrumental error.

"Bulk" oxygen isotope analysis at the University of Cape Town: The measurements were conducted using laser fluorination (a 20 W New Wave CO_2 laser mounted on a moveable stage), following the analytical protocol described by Harris and Vogeli (2010). The samples were measured in two measurement sessions a few months apart using two different fluorinating reagents. Between 1–3 mg of each apatite, sample was selected using a binocular microscope and weighed before loading into a highly polished, pure nickel, twelve-place sample holder, which was then heated in an oven at 110 °C for at least one hour. The samples were subsequently transferred to the reaction chamber. After pumping for > 2 h, about 10 kPa of BrF_5 (in the first session) or 20 kPa of ClF_3 (in the second session) was expanded into the reaction chamber for 30 s and then removed cryogenically. Following further pumping (> 30 min), a second load of 10 kPa BrF_5 (or 20 kPa ClF_3) was expanded into the reaction chamber and left overnight before extraction of oxygen from the samples was attempted. Each sample was reacted in the presence of ~ 10 kPa BrF_5 or ~ 20 kPa ClF_3. On completion of the reaction, the excess BrF_5 (ClF_3) and the free Br (Cl) formed by dissociation were frozen onto a cold finger, and the remaining gases were allowed to pass through a KCl trap maintained at about 200 °C in order to remove any remaining F_2. The gases were then expanded into a stainless-steel double-U trap immersed in liquid nitrogen, and the purified O_2 was collected onto a 5-Å molecular sieve contained in glass storage bottles. Each day, prior to oxygen extraction from the samples, a blank was run and the amount of gas was measured. The oxygen isotopic ratios were analysed off-line using a Finnigan DeltaXP mass spectrometer in the dual-inlet mode.

The measurements were calibrated using the reference sample MONGT garnet ($10^3\delta^{18}O_{VSMOW}$ = +5.38, Harris and Vogeli 2010), which had been calibrated against UWG-2 garnet ($10^3\delta^{18}O_{VSMOW}$ = +5.8, Valley *et al.* 1995). Two chips of MONGT were analysed along with every twelve samples. The long-term difference in $10^3\delta^{18}O_{VSMOW}$ values between MONGT duplicates is 0.115, which corresponds to a 2*s* of 0.15 (*n* = 283).

Yields of O_2 from apatite ranged from 36 to 109% (Appendix S6); those yields were determined from the mass 32 voltage in comparison with MONGT, which has a yield of 13.92 µmol O_2 per mg. The low yields resulted from the loss of apatite during lasing – unusually sensitive behaviour of apatite to the laser heating process was observed. In addition, most analysed apatite specimens were found to contain solid residues that did not react. Under the optical microscope, these appeared as small round spheres resembling glass,

and SEM-EDS analyses revealed that their main components were Ca and F (presumably fluorite).

"Bulk" oxygen isotope analysis at the Georg-August Universität, Göttingen: The extraction line that was used for fluorination and subsequent purification of O_2 is described in detail by Pack *et al.* (2016). The extraction was performed by infrared laser fluorination with BrF_5 as the oxidation agent. About 2 mg of each apatite sample as well as SARM 32 were placed in an eighteen-place sample holder and reacted in an atmosphere of ~ 4.5 kPa BrF_5. After reaction, excess BrF_5 was cryo-trapped, and traces of F_2 were reacted using NaCl to produce Cl_2. The purified O_2 sample was then transferred for ~10 min to a trap filled with 5-Å molecular sieve beads. The sample O_2 was then transported with a He carrier gas stream (10–20 ml min^{-1}) using a Hewlett Packard 5890 Series II gas chromatograph for separation of O_2 from contaminating NF_3 and N_2. The gas chromatograph was equipped with a 3.175-mm, 3-m long, packed 5-Å molecular sieve column; separation was conducted at 50 °C. Before each run, the gas chromatograph column was heated for 10 min to 250 °C. Before expanding the sample O_2 gas into the sample bellows of a Thermo MAT253 gas source isotope ratio mass spectrometer, the sample and a molecular sieve were heated to ~ 90 °C. The gas was then automatically measured in the dual-inlet mode relative to the reference gas in four successive blocks (twenty cycles with 8 s counting time for sample and reference gas)
for ~ 90 min.

The measurements were calibrated using two reference materials – San Carlos olivine ($10^3\delta^{18}O_{VSMOW2}$ = +5.12, Pack *et al.* 2016) and UWG2 garnet ($10^3\delta^{18}O_{VSMOW}$ = +5.8, Valley *et al.* 1995). The $\Delta'^{17}O$ data were normalised assuming a mean $\Delta'^{17}O$ value of San Carlos olivine of -52 ppm (established by Pack *et al.* (2016), Sharp *et al.* (2016), and Wostbrock *et al.* (2020) relative to O_2 extracted from VSMOW2 and SLAP2 water) and UWG2 garnet of -61 ppm (Miller *et al.* 2020, Wostbrock *et al.* 2020). Yields of O_2 from apatite range from 83 to 97% (Appendix S6).

For the additional test of tooth enamel of a modern African elephant (AG-LOX), powdered samples were chemically and thermally pre-treated, and they were subsequently analysed following the laser fluorination analytical protocol described above and the Ag_3PO_4-TC/EA measurement protocol described in Appendix S7.

"Bulk" oxygen isotope analysis at the University of Lausanne: The measurements of the apatite samples and SARM 32 were made using a method similar to that described by Vennemann *et al.* (2001). A few crystals from

each apatite sample were powdered and subsequently between 1.5 to 2.5 mg was loaded onto a small Pt-sample holder and pumped out to a vacuum of ~ 10^{-7} kPa. In order to assure that a zero-blank was approached, overnight pre-fluorination of the sample chamber and a shorter, 10-minute pre-fluorination prior to analyses were performed. The samples were then heated with a CO_2-laser in 5 kPa of pure F_2. Excess F_2 was separated from the O_2 produced by reaction with KCl held at 150 °C, producing Cl_2 gas that was frozen onto a liquid nitrogen trap. The extracted O_2 was collected on a molecular sieve (13X) with liquid nitrogen and subsequently expanded at about 50 °C into the dual-inlet of a MAT 253 isotope ratio mass spectrometer.

The measurements were calibrated using two reference materials – NBS-28 (quartz; $10^3\delta^{18}O_{VSMOW} = +9.64$, Coplen et al. 1983) and LS-1 (in-house quartz reference sample; $10^3\delta^{18}O_{VSMOW} = +18.1$, Seitz et al. 2017). Replicate measurements of these reference samples had mean uncertainties of ± 0.1 (1s) or better, and biases of $10^3\delta^{18}O_{VSMOW}$ values were less than ± 0.2 (1s) as compared with the assigned $\delta^{18}O$ value for NBS-28.

Oxygen yields were monitored based on the expected amounts of O_2 (in micromoles), which were calculated based on the weight of the sample and the chemical composition of apatite. The yields were then calibrated against the micromoles of O_2 measured for the coarse-grained LS-1 quartz (an internal reference sample) using the m/z 32 signal of the mass spectrometer at a constant inlet volume. In the case of the phosphates analysed in this study, only two samples (duplicates) were loaded with three or four quartz reference materials in the common reaction chamber; the $\delta^{18}O$ values of the phosphates were only accepted if the yields were 100 ± 4% (Appendix S6).

Results and discussion

Chemical compositions

EPMA major and trace element data collected using two different electron beam current settings (5 nA and 40 nA) document that the four studied apatite samples represent different members of $Ca_{10}(PO_4)_6(F, Cl,OH)_2$ solid solution series. All four samples have a variety of substitutions in all structural positions (Table 3 and 4), which is a feature typical for most natural specimens (e.g., Pan and Fleet 2002). None of the studied samples, however, has been shown to be particularly enriched in OH (Figure 3). The OH content was calculated based on the 5-nA dataset with the assumption that F + Cl + OH = two atoms per formula unit (Table 3).

Median values (based on 59–80 individual measurements) indicate that fluorapatite MGMH#128441A is the most OH-enriched sample in this set, while others are either pure fluorapatite end-member (MZ-TH) or contain only traces of hydroxyl component (MGMH#133648 and ES-MM). The datasets for MGMH#133648 and MGMH#128441A were previously presented and discussed by Wudarska et al. (2021) who described reference materials for chlorine isotope ratio measurement. It was noted there that the chlorine mass fraction of MGMH#133648 varies depending on the electron beam current settings (6.34 ± 0.16% m/m (1s) and 6.09 ± 0.71% m/m (1s) for 5 and 40 nA, respectively). Grain-to-grain variations were detected in the 40 nA measurement sessions (only), which may be related to the crystal orientation effect that is commonly observed in EPMA studies of apatite (e.g., Stormer et al. 1993, Goldoff et al. 2012). However, the SEM-based investigation of the inclusions showed that chlorapatite MGMH#133648 contains OH-enriched areas (see "Sample selection and description") that could also be the reason for grain-to-grain variations.

Our EPMA datasets indicate a wide range of cationic and anionic substitutions in the structural positions dominated by Ca^{2+} and PO_4^{3-}. Fluorapatite MGMH#128441A is very rich (1.74% m/m) in low atomic number rare earth elements (LREE: La^{3+}, Ce^{3+}, Pr^{3+}, Nd^{3+}). The other samples contain lower amounts of such elements (0.32% m/m in MGMH#133648 and 0.69% m/m in MZ-TH) or, in the case of ES-MM, no LREE were detected in the crystal structure. MGMH#128441A also contains trace amounts of Fe, Mn, and Mg, while Sr and Na were detected in all four samples. Moreover, the incorporation of small amounts of SiO_4^{4-} and SO_4^{2-} were identified in MGMH#133648, MGMH#128441A, and MZ-TH. Fluorapatite ES-MM, which is generally poor in trace elements, only contains the Si component. Consequently, the mole fraction of Ca+P (X_{Ca+P}), calculated as the ratio of Ca+P versus the sum of all other components of each apatite specimen (listed in Table 4 plus H_2O mass fraction from Table 3), has the highest value for ES-MM (0.99) and the lowest for MGMH#128441A (0.92). Both MGMH#133648 and MZ-TH have X_{Ca+P} values close to 0.96.

Substitution of CO_3^{2-} and OH^- in the apatite structure

Based on the results obtained using infrared spectroscopy (Figure 4) and thermogravimetry coupled with mass spectroscopy (Figure 5), we tried to identify the molecular species present in our samples. In the apatite structure, CO_3^{2-} and OH^- are the two components that dominantly

Table 3.
EPMA major element data for the studied apatite samples, using 15 kV, 5 nA and 10 μm beam parameters

Sample ID	MGMH#133648		MGMH#128441A		MZ-TH		ES-MM	
n	59		60		80		80	
	median	1 *s*	median	1 *s*	median	1 *s*	median	1 *s*
P_2O_5	41.36	0.45	40.53	0.48	41.02	0.42	41.47	0.45
SiO_2	0.12	0.04	0.52	0.06	0.09	0.04	0.13	0.05
SO_3	0.09	0.04	0.11	0.04	0.23	0.07	< DL	
CaO	54.21	0.46	53.47	0.63	54.18	0.49	55.33	0.39
SrO	0.09	0.04	0.04	0.03	0.49	0.05	0.05	0.04
FeO	< DL		0.09	0.06	< DL		< DL	
MnO	< DL		0.15	0.06	< DL		< DL	
Na_2O	0.07	0.05	0.18	0.05	0.21	0.07	0.09	0.04
F	< DL		2.15	0.13	3.76	0.18	3.34	0.17
Cl	6.34	0.16	0.99	0.08	< DL		0.07	0.03
H_2O	0.15	0.04	0.47	0.06	–		0.17	0.08
-O(F)	0.00		0.91	0.05	1.58	0.07	1.41	0.07
-O(Cl)	1.43	0.04	0.22	0.02	0.00		0.02	0.01
Total	100.99	0.76	97.56	1.01	98.39	0.62	99.22	0.48
Structural formulae $M_{10}(TO_4)_6X_2$								
Ca	9.93		9.89		9.94		10.05	
Sr	0.01		0.00		0.05		0.00	
Fe	–		0.01		–		–	
Mn	–		0.02		–		–	
Na	0.02		0.06		0.07		0.03	
∑M	**9.96**		**9.99**		**10.05**		**10.09**	
P	5.99		5.93		5.94		5.95	
Si	0.02		0.09		0.02		0.02	
S	0.01		0.01		0.03		–	
∑T	**6.02**		**6.03**		**5.99**		**5.98**	
F	–		1.17		2.04		1.79	
Cl	1.84		0.29		–		0.02	
OH	0.16		0.54		–		0.19	
∑X	**2.00**		**2.00**		**2.04**		**2.00**	

< DL – below detection limit.
The data represent median values (% *m/m*) of 59–80 individual measurements (*n*) conducted on a total of fifteen or twenty fragments of each material embedded in Mounts #1 and #2 (Figure 2). H_2O and OH components were calculated based on ideal stoichiometry. The data for MGMH#133648 and MGMH#128441A were originally published by Wudarska *et al.* (2021). For the full EPMA datasets and the detection limits see Appendix S8.

contribute to mass loss during heating, resulting in CO_2 and H_2O release. As a result of our IR and TG-MS experiments, trace amounts of OH^- were detected in all four samples (Figures 4a and 5b), whereas CO_3^{2-} was identified in only MZ-TH and ES-MM (Figures 4b, c and 5c). The IR spectra of ES-MM indicated two types of carbonate substitution: CO_3^{2-} located in monovalent F^-/Cl^-/OH^- position in the apatite channel (A-type) and in tetrahedral PO_4^{3-} anions positions (B-type). In contrast, the IR spectra of MZ-TH showed only A-type of CO_3^{2-} substitution (Figure 4b, c; Regnier *et al.* 1994, Tacker 2008). Unlike carbonated hydroxylapatite experiencing 6–10% *m/m* loss in similar TG-MS experiments (Leventouri *et al.* 2000, Tõnsuaadu *et al.* 2003), the apatite samples tested in this study showed only small total mass losses ($Δm_{total}$) amounting to 0.11–0.26% *m/m*, which we

calculated from TG curves obtained by heating powdered samples up to 1000°C (Figure 5). Chlorapatite MGMH#133648 and Cl^-- and OH^--enriched fluorapatite MGMH#128441A showed higher $Δm_{total}$ and lower temperature of thermal decomposition than the two other samples – MZ-TH and ES-MM – which represent almost pure fluorapatite end-members. This result indicates lower thermal stability of apatite containing Cl^- and/or OH^- and is consistent with previously established the fluorapatite–chlorapatite–hydroxylapatite order of apatite thermal stability (Tõnsuaadu *et al.* 2012).

IR-DRIFT spectra collected on the products of heating to 1000 °C (the residues from the thermogravimetric experiments; Appendix S9) showed that all tested apatite samples

Table 4.
EPMA major and trace element data for the studied apatite samples, using 15 kV, 40 nA and 10 μm beam parameters

| Sample ID	MGMH#133648		MGMH#128441A		MZ-TH		ES-MM	
n	45		45		45		45	
	median	1s	median	1s	median	1s	median	1s
P_2O_5	40.96	0.20	41.17	0.13	41.45	0.23	42.07	0.15
SiO_2	0.12	0.02	0.53	0.03	0.09	0.02	0.12	0.03
SO_3	0.11	0.02	0.19	0.02	0.20	0.05	< DL	
Y_2O_3	< DL		0.10	0.02	< DL		< DL	
La_2O_3	0.06	0.03	0.44	0.06	0.16	0.05	< DL	
Ce_2O_3	0.14	0.04	0.89	0.08	0.34	0.09	< DL	
Pr_2O_3	< DL		0.09	0.05	<DL		< DL	
Nd_2O_3	0.09	0.04	0.32	0.06	0.16	0.06	< DL	
CaO	53.62	0.33	53.50	0.24	55.01	0.27	55.69	0.23
SrO	0.11	0.01	0.04	0.02	0.50	0.03	0.05	0.01
FeO	< DL		0.10	0.02	< DL		< DL	
MnO	< DL		0.14	0.02	< DL		< DL	
MgO	< DL		0.04	0.01	< DL		0.02	0.01
Na_2O	0.06	0.01	0.20	0.02	0.20	0.05	0.09	0.02
F	< DL		2.36	0.12	4.28	0.20	3.71	0.23
Cl	6.09	0.71	1.03	0.02	0.00	0.00	0.05	0.00
-O(F)	0.00	0.00	0.99	0.05	1.80	0.09	1.56	0.10
-O(Cl)	1.37	0.16	0.23	0.00	0.00	0.00	0.01	0.00
Total	100.00	0.77	99.91	0.36	100.68	0.29	100.27	0.30

< DL – below detection limit.
The data represent median values (% *m/m*) of forty-five individual measurements (*n*) conducted on fifteen fragments of each apatite sample embedded in Mounts #1 and #2 (Figure 2). The data for MGMH#133648 and MGMH#128441A were originally published by Wudarska *et al.* (2021). For the full EPMA datasets and the detection limits see Appendix S8.
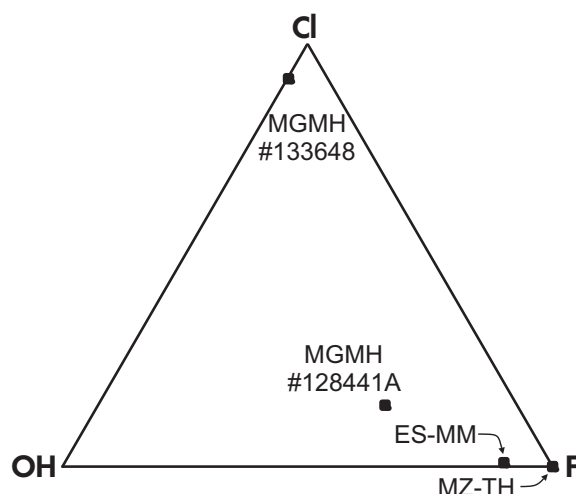
Figure 3. Ternary diagram showing median F–Cl–OH compositions of the studied samples determined by EPMA (Table 3).

underwent complete lattice water decomposition and partial OH⁻ group decomposition; the characteristic OH⁻ group bands disappeared almost completely for MGMH#133648 and MZ-TH. To remove all OH⁻ groups from hydroxylapatite, it is necessary to heat up to 1300 °C (Tõnsuaadu *et al.* 2012); however, the temperature depends on various physicochemical properties of apatite structure (Elliott 1994). Furthermore, the sharp slope of TG curves without a plateau up to 1000 °C (Figure 5) also indicates that the dehydroxylation and decarbonation reactions were not complete at 1000 °C. In fact, the IR-DRIFT spectra of MZ-TH and ES-MM products of heating to 1000 °C (Appendix S9) revealed the presence of CO_3^{2-} bands with slightly reduced intensities. The ES-MM sample underwent complete decomposition of CO_3^{2-} substituted in monovalent F⁻/Cl⁻/OH⁻ position (A-type, Tacker 2008), indicating higher thermal stability of B-type carbonate substitution in tetrahedral PO_4^{3-} anion position of igneous apatite structure. The temperature of the TG experiment was, however, limited by the maximum 1000 °C temperature tolerated by the Pt sample crucible holders used for heating the apatite. Further details on TG-MS and IR results are shown in Appendix S9. Despite the fact that quantitative determination of OH⁻ and CO_3^{2-} was not achieved due to their incomplete decomposition and the overlapping peaks on TG and MS curves, the IR and TG data provided a
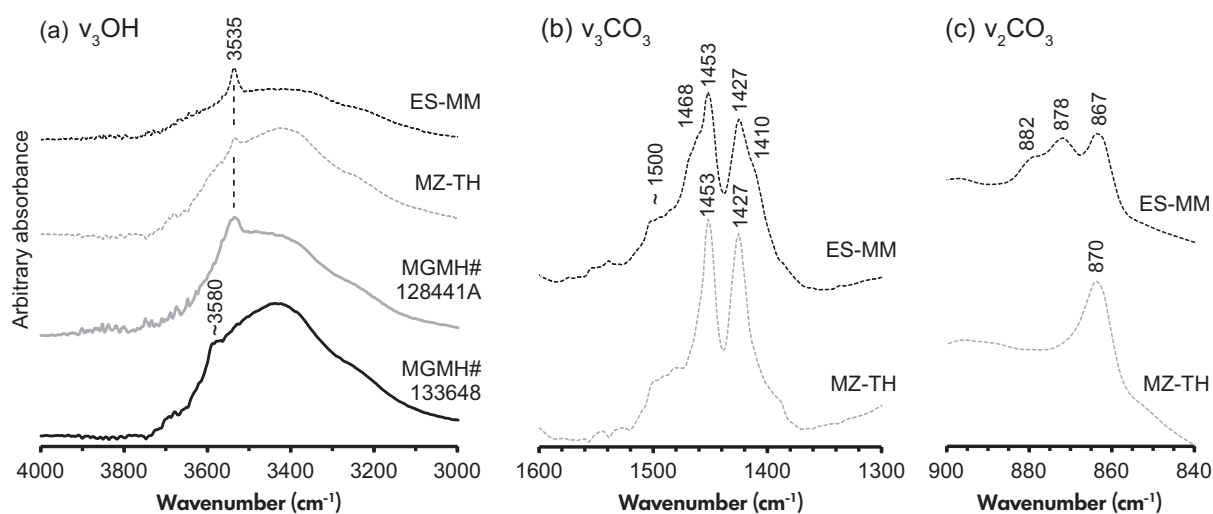
Figure 4. DRIFT spectra of tested apatite samples in the regions of OH- stretching (a), CO_3^{2-} stretching (b) and CO_3^{2-} bending (c) modes. For detailed interpretation of the IR data, see Appendix S9.

detailed picture of the extent of incorporation of these species in all four studied apatite samples.

Estimation of phosphate-bonded and "bulk" oxygen contents

Carbonate substitution in minerals of the apatite group has a significant impact on their properties (e.g., solubility, thermal stability) and commonly occurs not only in calcium phosphate (Chickerur *et al.* 1980, Regnier *et al.* 1994, Tacker 2008) but also in lead phosphate and lead arsenate members of this group (Kwaśniak-Kominek *et al.* 2017, Lempart *et al.* 2019). While CO_2 contents in most inorganic apatite crystals are well below 1% *m/m* (e.g., Santos and Clayton 1995, Tacker 2008), biogenic apatite commonly incorporates 4–6% *m/m* of CO_2 (e.g., Elliott 1994), and carbonate-rich fluorapatite in phosphorite rocks has been reported to have up to 6% *m/m* of CO_2 (e.g., Shemesh *et al.* 1988). GS-IRMS data acquired on two specific components – PO_4^{3-} ($\delta^{18}O_{PO4}$) and CO_3^{2-} ($\delta^{18}O_{CO3}$) – in such carbonate-rich apatite specimens have shown that their isotopic compositions can vastly differ from each other, for example, structural carbonate in mammalian enamel and bone apatite has been reported to be ~ 8.7 ‰ more enriched in ^{18}O than the corresponding phosphate component (Bryant *et al.* 1996) and in fluorapatite from sedimentary phosphorite rocks, such enrichment has been reported to reach 12.4 ‰ (Shemesh *et al.* 1988). To our knowledge, there are no data available for $\delta^{18}O_{PO4}$ and $\delta^{18}O_{CO3}$ measurements in igneous or metamorphic apatite samples such as those studied here. Furthermore, oxygen isotope compositions of other anions incorporated in the apatite structure (e.g., OH⁻, SiO_4^{4-}, and SO_4^{2-}) have not been reported in previous studies. If these

components react differently to post-crystallisation processes (e.g., diagenesis), studied samples may be isotopically complex, and "bulk" isotope values may not give the full picture (Kohn *et al.* 1999).

SIMS measurements of apatite samples cannot discriminate between different oxygen components inherently providing information only on pooled isotope compositions. Therefore, we tried to estimate the concentrations of oxygen associated with different anion groups based on our EPMA, TG, and IR datasets (Table 5) in order to assess their relative contribution to the "bulk" $\delta^{18}O$ data. Total mass losses (from 0.10 to 0.26% *m/m*, Table 5) estimated in TG experiments correspond to partial OH⁻ and CO_3^{2-} decomposition in the apatite structure with also a minor contribution of adsorbed water (0.076% *m/m* in MGMH#128441A, while negligible in the other three samples). These results indicate only trace amounts of carbonate and hydroxyl components in all four apatite samples. Three of the studied samples (MGMH#133648, MZ-TH, ES-MM) have ~ 99% of P-bonded oxygen as revealed by EPMA data. In contrast, MGMH#128441A, which has a more complicated crystal chemistry, has ~ 96% of P-bonded oxygen. The OH⁻ contents in our four apatite samples may be overestimated as they were calculated with the assumption that the X-site is fully occupied by F⁻, Cl⁻ or OH⁻, disregarding the possibility of any vacancies (e.g., Pan and Fleet 2002). Moreover, the OH⁻ calculations based on EPMA do not include the A-type substitution of CO_3^{2-} that was detected using IR in the fluorapatite ES-MM. TG and IR datasets indicate only minor amounts of OH⁻ (maximum mass loss of ~ 0.2% *m/m*) in MGMH#128841A, while the OH⁻ content calculated based on EPMA data is ~four times higher. It has previously
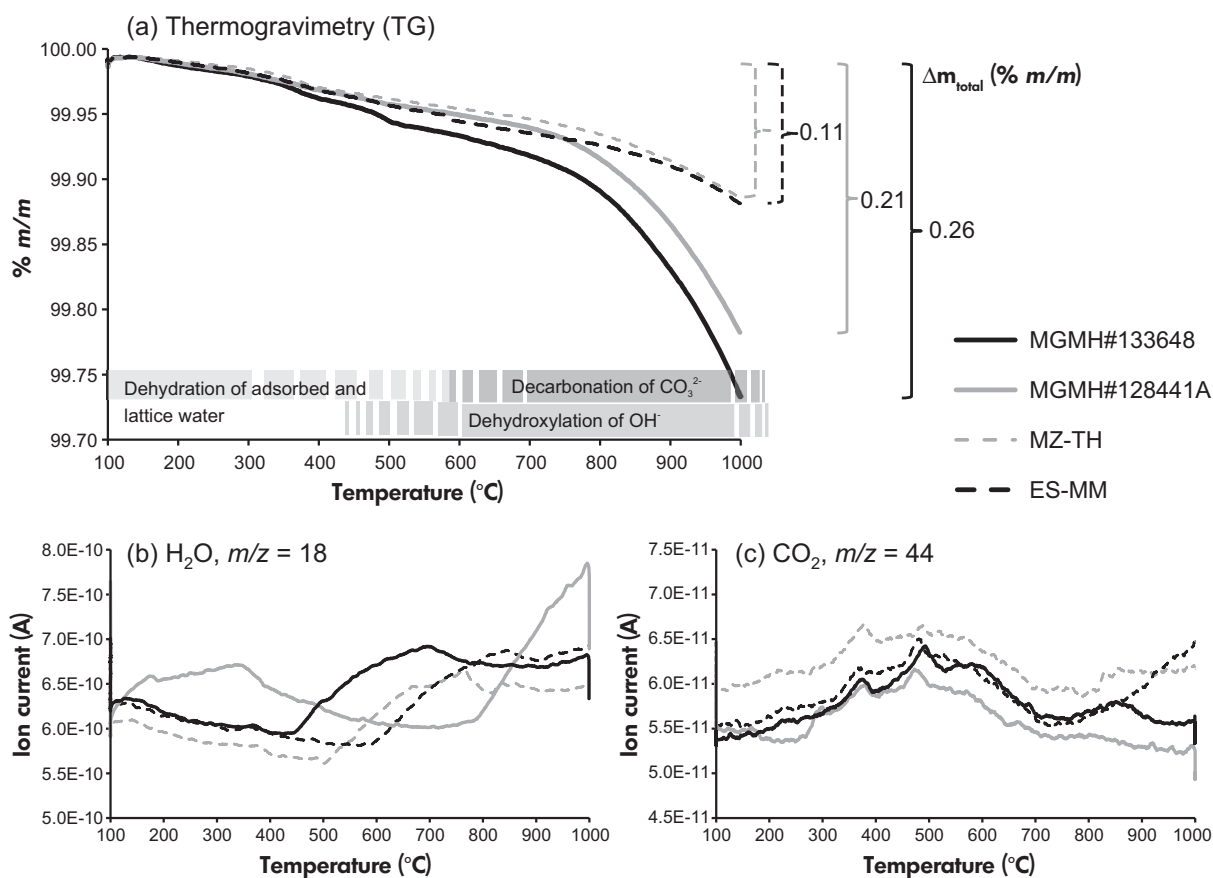
Figure 5. (a) TG curves of tested apatite samples combined with (b) H$_2$O, m/z = 18 and (c) CO$_2$, m/z = 44 MS spectra obtained using a heating rate of 20 °C min^{-1} in a nitrogen gas atmosphere. For detailed interpretation of the TG-MS data, see Appendix S9.

been shown that the apatite from this location (Eagle County, Colorado) has O^{2-} or O$_2^{2-}$ in the X-site (Young and Munson 1966), but whether such a substitution occurred in MGMH#128441A would require further studies. CO$_3^{2-}$ ions are also incorporated in the tetrahedral anion position of PO$_4^{3-}$ in ES-MM and MZ-TH; it should be noted that the estimated contribution of oxygen associated with PO$_4$ is slightly overestimated in these two fluorapatite specimens. Nonetheless, the most important conclusion from this portion of our study is that oxygen-bearing components, other than PO$_4^{3-}$, are incorporated in the apatite structure only at trace levels, and the contribution of P-bonded oxygen in all studied samples is significantly higher than the ~ 85% estimated for bioapatite samples (Kohn and Cerling 2002).

SIMS homogeneity test of ^{18}O/^{16}O ratios

Two homogeneity tests conducted on random apatite fragments from each apatite sample (Mounts # 1–3, Figure 2)

confirmed that they are sufficiently homogeneous at the sub-nanogram sampling scale in terms of their oxygen isotopic composition to be appropriate for testing. The repeatability of between twenty-one and fifty-one measurements performed on between nine and twenty fragments was in all four cases better than ± 0.25 ‰ (1s, Table 6, Figure 6a–i). This variability is about two to three times higher than the mean uncertainty of a single ^{18}O/^{16}O determination (± 0.09 ‰; 1SE of twenty 4-second integrations) and may, thus, reflect a real but modest degree of sample heterogeneity.

An additional test conducted on a piece of white, OH-rich crust removed from the surface of MGMH#133648 (Mount #4, Appendix S2) showed a significantly larger isotopic variation towards 2.9 ‰ higher ^{18}O/^{16}O ratios than the volumetrically dominant, transparent, yellow-coloured, OH-poor crystals (Table 6, Figure 6j). Similar observations were made for the chlorine isotopes in the study by Wudarska et al. (2021) based on SIMS ^{37}Cl/^{35}Cl measurements from the same sample mount. The white crust

Table 5.
Estimated concentrations of oxygen associated with different anion groups (calculated based on EPMA data; Table 3) and a summary on OH$^-$ and CO$_3^{2-}$ substitutions in the apatite structure (TG and IR analyses; Figures 4 and 5, Appendix S9)

Sample ID	EPMA				TG	IR
	Oxygen in PO$_4^{3-}$ (% m/m)	Oxygen in SiO$_4^{4-}$ and SO$_4^{2-}$ (% m/m)	Oxygen in OH$^-$ (% m/m)	Percentage of P-bonded oxygen in total oxygen concentration	Δm_{total}[a] (% m/m)	CO$_3^{2-}$ substitution[b]
MGMH#133648	36.98	0.19	0.25	98.8%	0.26	< DL
MGMH#128441A	37.73	0.64	0.83	96.2%	0.21	< DL
MZ-TH	37.60	0.29	< DL	99.2%	0.11	B-type
ES-MM	37.87	0.13	0.29	98.9%	0.11	A- and B-type

< DL – below detection limit.

[a] Total mass losses in thermogravimetric experiments correspond to OH$^-$ and CO$_3^{2-}$ decomposition in the apatite structure below 1000°C (Figure 5).

[b] CO$_3^{2-}$ substitution types: A- in monovalent F$^-$/Cl$^-$/OH$^-$ position and B- in tetrahedral PO$_4^{3-}$ position of Ca$_{10}$(PO$_4$)$_6$(F, Cl,OH)$_2$ (Figure 4).

was cut from the MGMH#133648 prior to crushing, but small amounts are still present in the split material. These heterogeneities were not detected in the SIMS tests of random fragments (Mount #1 and #3), perhaps because micro-areas enriched in OH, if present in a crystal fragment, are preferentially removed during the polishing process.

In the chlorine isotope study of apatite by Wudarska *et al.* (2021), as well as in earlier works of Huberty *et al.* (2010) and Kita *et al.* (2011) on magnetite, haematite, and sphalerite, a crystallographic orientation effect on measured isotope ratios had been noted in SIMS data. In order to assess if such an effect also occurs in the case of ^{18}O/^{16}O measurements in apatite, we analysed three Durango fluorapatite chips that were intentionally embedded in Mount #5 (Appendix S3) so as to provide differing crystallographic orientations: perpendicular to the *c*-axis (Dur-A), parallel to the *c*-axis (Dur-B), and an intermediate orientation (Dur-C). Our test was performed on the same mount that was used in the chlorine study by Wudarska *et al.* (2021), where the details of EBSD determination of crystallographic orientations can be found. The anisotropic behaviour of apatite during ^{37}Cl/^{35}Cl measurements results from the incorporation of Cl$^-$ in the anion column parallel to the c-axis of the hexagonal structure. In the case of oxygen, which is dominantly incorporated in the tetrahedral PO$_4^{3-}$ position, no crystallographic orientation effect was observed (Table 6, Figure 6k). This conclusion parallels the results of the recent study by Li *et al.* (2021) who also demonstrated a lack of such an effect in SIMS measurements of oxygen isotopes in apatite.

δ^{18}O values determined by GS-IRMS

GS-IRMS analyses of oxygen isotopes have been successfully applied to various biological and inorganic calcium phosphates for decades, making it possible to advance our knowledge on both environmental conditions in the Earth's history as well as on the physiological characteristics of extinct fauna (e.g., Lécuyer *et al.* 1993, Joachimski *et al.* 2009, Quinton and MacLeod 2014). Over the course of many years of apatite studies, the analytical protocols for oxygen isotope measurement have been tested and improved to achieve the best quality data, but complications arise in comparing results obtained using differing analytical strategies.

Biogenic apatite is the most commonly analysed phosphate material, and due to extensive anionic substitution in the crystal structure (e.g., PO$_4^{3-}$, CO$_3^{2-}$, OH$^-$) and potential interferences of differing isotope signatures of various components, δ^{18}O determinations of chemically isolated PO$_4$ fractions is the most commonly applied strategy in palaeoenvironmental studies. Vennemann *et al.* (2002) demonstrated that δ^{18}O values obtained from the reaction of Ag$_3$PO$_4$ with graphite in a continuous flow TC/EA agree well with the results of conventional fluorination analyses of the same material. In this current contribution, however, we compare the results of phosphate-bonded oxygen analyses (Ag$_3$PO$_4$-TC/EA) with the "bulk" oxygen data obtained by laser fluorination of unprocessed apatite samples. The main goal of our work was to characterise new reference materials for calibration of SIMS measurements, which provide information on "bulk" oxygen isotope compositions of polished apatite specimens.

The four apatite samples that are the focus of this study have a wide range of oxygen isotope compositions with mean $10^3\delta^{18}$O$_{VSMOW}$ values falling between +5.8 and +21.7 (Table 7). However, we observe non-systematic variations between the GS-IRMS datasets (Figure 7) that

Table 6.
Results of SIMS homogeneity tests

| Sample ID	Number of fragments	Number of analyses	Mean $^{18}O/^{16}O$ ratio[a]	Repeatability 1s [‰]	
Randomised analyses on random apatite grains in Mounts #1 and #2 (22–23 June and 25–26 June 2018)					
MGMH#133648	12	28	0.0020286(5)	0.25	
MGMH#128441A	15	37	0.0020339(4)	0.18	
Dur-1[b]	1	15	0.0020370(4)	0.18	
NIST SRM 610-1[b]	1	15	0.0020265(4)	0.18	
MZ-TH	18	41	0.0020453(5)	0.24	
ES-MM	20	39	0.0020719(3)	0.12	
Dur-2[b]	1	18	0.0020429(2)	0.12	
NIST SRM 610-2[b]	1	18	0.0020318(3)	0.13	
Randomised analyses on random apatite grains in Mount #3 (11–12 September 2020)					
MGMH#133648	10	50	0.0020376(4)	0.20	
MGMH#128441A	9	50	0.0020414(4)	0.18	
MZ-TH	10	51	0.0020466(4)	0.20	
ES-MM	13	49	0.0020722(5)	0.24	
Dur-3[b]	3	14	0.0020444(3)	0.16	
NIST SRM 610-3[b]	1	22	0.0020321(3)	0.17	
Analyses of targeted OH-rich and OH-poor areas in chlorapatite in Mount #4 (4 November 2019)					
MGMH#133648 OH-poor	-	19	0.0020361(6)		
MGMH#133648 OH-rich	-	21	0.0020370(15)	0.61	
NIST SRM 610-4[b]	1	10	0.0020313(4)	0.19	
Analyses of the oriented crystal fragments in Mount #5 (20 February 2020)					
Dur-A	1	10	0.0020391(2)	0.11	
Dur-B	1	10	0.0020395(4)	0.21	0.17
Dur-C	1	10	0.0020395(3)	0.14	
NIST SRM 610-5[b]	1	8	0.0020277(4)	0.20	

For full datasets of all individual analyses, see Appendix S10.

[a] Not corrected for IMF. Uncertainties given in brackets (1s) refer to the least significant digits of the mean values.

[b] Instrumental drift monitor analyses regularly interspersed with analyses of the studied apatite samples. Dur-1, Dur-2, NIST SRM 610-1, NIST SRM 610-2, NIST SRM 610-3, NIST SRM 610-4 indicate random fragments of the Durango apatite and NIST SRM 610 glass, which were used for monitoring the instrumental drift. During the analytical sessions in June 2018 and November 2019, instrumental drift was observed, and therefore, the data collected within these sessions was corrected based on closely spaced analyses of NIST SRM 610 fragments.

do not correspond to the phosphate-bonded and "bulk" oxygen contents estimated based on EPMA, TG, and IR (Table 5). Determined $10^3\delta^{18}O_{VSMOW}$ values are method-specific and they differ in magnitude by up to 1.67 (MGMH#133648). The carbonate contents in all four apatite specimens are negligible compared with those commonly detected in biological samples, in which $\delta^{18}O_{VSMOW}$ values determined for structural carbonate are usually higher than those measured for the corresponding phosphate component (Bryant *et al.* 1996, Kohn and Cerling 2002). It is possible that carbonate substitutions as well as other chemical characteristics of the four samples studied here could, at least in part, be responsible for the differences between the datasets. However, fluorapatite MGMH#128441A, which has a variety of anionic substitutions (OH⁻, SiO_4^{4-}, and SO_4^{2-}) and only ~96% of P-bonded oxygen, has the second smallest difference between the phosphate and the "bulk" mean $10^3\delta^{18}O_{VSMOW}$ results.

Moreover, chlorapatite MGMH#133648 has been found to be heterogeneous in the SIMS test of Mount #4, where we compared OH-rich and OH-poor areas. This additional test was performed specifically to assess the isotopic signature of the whitish crust that was discarded in the mineral separation; we felt this test was important because minor amounts of the hydroxyl material could remain present in the final splits for the gas source investigations. Such heterogeneities were not recorded in the SIMS tests of random crystals (Mounts #1 and 3), perhaps because micro-areas enriched in OH, if present in a crystal fragment, might be more easily removed during the sample preparation process. The "bulk" LF measurements were performed on the apatite crystals that were carefully hand-picked from the produced splits beforehand in order to eliminate non-apatite inclusions and coatings (including OH-rich parts, which are usually white/opaque and can easily be distinguished from volumetrically dominant yellow transparent crystals). The hand-picking work was done under a binocular microscope,
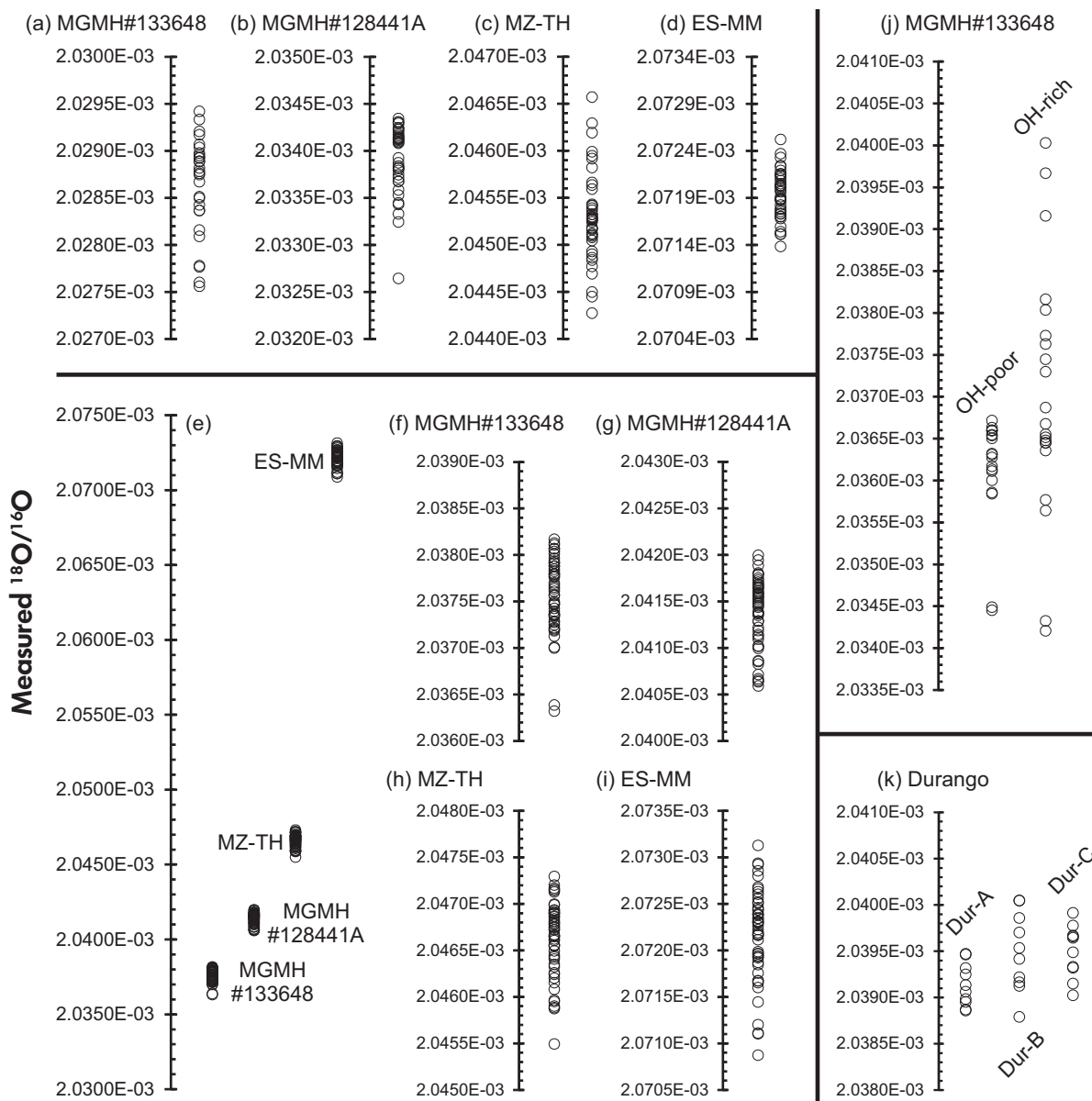
Figure 6. Individual $^{18}O/^{16}O$ measurements by SIMS (not corrected for IMF). Graphs (a–d) represent the analyses of random fragments from four apatite samples embedded in Mounts #1 and #2. Graph (e) represents the analyses of random fragments embedded in Mount #3, while graphs (f–i) show expanded charts of these samples from graph (e). Graph (j) represents the results of an additional test of selected areas in MGMH#133648 crust (Appendix S2), showing that the oxygen isotope ratios of OH-rich areas overlap with those measured in OH-poor parts of this chlorapatite specimen, but their mean ratios are significantly different. The data included in graphs (a–d, j) were corrected for instrumental drift based on regularly repeated, closely spaced analyses of NIST SRM 610. Graph (k) shows the results of the measurements conducted on three Durango apatite fragments having different crystallographic orientation with respect to *c*-axis.

so micro-areas enriched in OH might have still been present in the analysed material. Nonetheless, all three LF laboratories agree well on the $10^3\delta^{18}O_{VSMOW}$ value for the chlorapatite MGMH#133648 (+4.97 ± 0.21, 1*s*). That

value is, though, significantly lower than the corresponding value reported by Ag_3PO_4-TC/EA laboratories (+6.64 ± 0.22, 1*s*). Despite the OH-related issues noticed in the SIMS investigation, this sample is the only one in our

study for which both methods (Ag_3PO_4-TC/EA and LF) have a relatively small spread of $\delta^{18}O$ results.

We could not correlate the non-systematic offsets between the GS-IRMS datasets produced by different laboratories with the differences between analytical protocols applied. Although each group of methods (Ag_3PO_4-TC/EA and LF) is based on similar principles, the analytical protocols, which may contribute to overall laboratory bias, differ in many details. This includes not only various sample pre-treatment strategies, chemistry of reagents, solution concentrations, and types of mass spectrometers, but most importantly the reference materials used for calibration of GS-IRMS measurements (Table 2). A recent study by Pederzani *et al.* (2020), which was published after we had completed our data collection, showed that NaOCl pre-treatment may alter the original isotopic composition of apatite. In one of the Ag_3PO_4-TC/EA laboratories (at Uni. Missouri), such a pre-treatment was applied, but this fact does not explain the observed differences between the datasets, and due to their complexity, we are not able to assess if such an effect also occurred during sample preparation in our study.

Finally, in one of the LF laboratories (at Uni. Cape Town), it was noted that the apatite samples are much more challenging to analyse by laser fluorination compared with other routinely measured minerals (silicates or oxides). Apart from the problem of unreacted residue (see "Analytical methods" section), the apatite fragments were extremely sensitive during lasing, and a slight increase in laser power would send flaming fireballs of material shooting across the sample chamber. However, loss of the sample at these high temperatures seems not to cause much fractionation – the yields for chlorapatite MGMH#133648 were 36 and 62% corresponding to $10^3\delta^{18}O_{VSMOW}$ values of +4.80 and +4.99, respectively. Moreover, a change in a fluorinating reagent (ClF_3 instead of BrF_5) for the third measurement of this chlorapatite sample did not significantly influence the collected data, yielding a $10^3\delta^{18}O_{VSMOW}$ value of +5.32 (yield of ~ 47%). Despite such low yields estimated for some of the LF measurements, we did not observe any correlation between $10^3\delta^{18}O_{VSMOW}$ values and the corresponding yields (Appendix S6).

The phosphate rock SARM 32 was selected as a direct intercomparison material that was analysed along with the apatite samples in all six GS-IRMS laboratories. This material showed the largest data spread among studied samples (Table S5.2 and Figure S5.1 in Appendix S5); LF-determined $10^3\delta^{18}O_{VSMOW}$ values (+6.44 ± 0.37, 1s) are distinctly lower than those analysed by Ag_3PO_4-TC/EA

(+7.74 ± 0.61, 1s), and this offset fits the general trend for all of our samples. It has been noticed that SARM 32, sometimes, does not fully dissolve in 2 mol l^{-1} HNO_3. It is possible that mostly traces of phlogopite and vermiculite contribute to the observed undissolved residuum. It is not clear whether this could be the reason for comparatively poor repeatability for SARM 32, and caution is recommended regarding future use of this material as an RM for $\delta^{18}O$ measurements.

All of the observations based on the multiple GS-IRMS datasets collected using various analytical strategies suggest a more complex behaviour of apatite during sample processing for $\delta^{18}O$ analyses than other minerals, such as quartz and tourmaline or synthetic glasses, and highlights the importance of the characterisation of RMs with the support of multiple laboratories applying different protocols. Despite great efforts made by the gas source mass spectrometry community to collect high-quality data, where extreme care was paid to the calibration methodology, some disagreements still exist on the oxygen isotope values of widely used reference materials. This problem is illustrated by the fact that two different $10^3\delta^{18}O_{VSMOW}$ values (+21.7 and +22.6) have been suggested for Florida phosphate rock NBS120c (Lécuyer *et al.* 1993, Vennemann *et al.* 2002). While the reason for this difference is unknown, nowadays, the value of +21.7 (Lécuyer *et al.* 1993) is generally accepted.

The isotopic data reported for our apatite reference samples are subject to future revision as data generated by differing sample preparation and measurement strategies become harmonised, which, we believe, should happen owing to worldwide distribution and further characterisation of these and possibly other phosphate materials. The SIMS homogeneity tests showed that all four apatite samples are sufficiently homogeneous at the sub-nanogram sampling scale to serve as the reference material; repeatability was in all four cases better than ± 0.25 ‰ (1s, Table 6). However, the two fluorapatite specimens MZ-TH and ES-MM exhibit relatively large spread of LF-determined $10^3\delta^{18}O_{VSMOW}$ values (1s of ± 0.68 and ± 0.74, respectively) compared with the chlorapatite MGMH#133648 and the fluorapatite MGMH#128441A (1s of ± 0.21 and ± 0.25, respectively). The reason for higher uncertainty of MZ-TH measurements could be the fact that this sample contains minor amounts of non-apatite impurities, such as iron oxides and Fe–Mg aluminosilicates, that could have influenced $\delta^{18}O$ determinations of apatite. ES-MM, which is a gem-quality specimen, requires further investigation as to the source of the larger GS-IRMS data spread, especially given that the mean $10^3\delta^{18}O_{VSMOW}$ values determined by LF and

Ag_3PO_4-TC/EA methods are relatively close (+21.80 vs. +21.63), but two laboratories operating with different methods (Uni. Missouri and Uni. Lausanne) measured consistently higher values of approximately +22.4 for this material (Table 7).

Oxygen isotope composition of tooth enamel of a modern African elephant (AG-LOX)

Powdered tooth enamel of a modern African elephant (AG-LOX) was tested in two independent laboratories at the University of Göttingen in order to assess inter-laboratory bias for oxygen isotope measurements of biogenic apatite using LF and Ag_3PO_4-TC/EA methods.

The tests showed that the $10^3\delta^{18}O$ values determined using laser fluorination are typically ~0.98 lower than those obtained by TC/EA (Appendix S7). The $10^3\delta^{18}O$ value of Ag_3PO_4 precipitated from AG-LOX is +20.53 ± 0.79 (1s, $n = 28$) as determined by TC/EA, while the mean $10^3\delta^{18}O$ value from laser fluorination measurements ($n = 72$) is +19.55 ± 0.63 (1s). AG-LOX has previously been used as an internal reference material for oxygen and carbon isotopic analyses of apatite-bounded carbonate, and a $10^3\delta^{18}O$ value of +30.08 ± 0.08 (1s) has been published for this specific component (Gehler *et al.* 2012). In our study, however, powdered AG-LOX tooth enamel was chemically and thermally pre-treated prior to isotopic analyses (Appendix S7). This step was aimed at

Table 7.
$\delta^{18}O_{VSMOW}$ values determined by GS-IRMS for studied apatite samples

Sample ID	Analysis type	"phosphate" $10^3\delta^{18}O_{VSMOW}$ (Ag_3PO_4-TC/EA)			"bulk" $10^3\delta^{18}O_{VSMOW}$ (LF)		
	Laboratory	Uni Erlangen	Uni Lyon	Uni Missouri	Uni Cape Town	Uni Göttingen	Uni Lausanne
MGMH#133648	Aliquot 1	6.61	6.95	6.92	4.99	4.74	5.30
		6.50	7.05	6.41			
		6.75	6.95	5.6[a]			
		6.50	6.58				
		7.05					
		6.74					
		6.35					
		6.50					
		6.74					
		6.35					
	Aliquot 2	6.64		6.40	4.80		4.99
		6.68		6.21			
		6.32					
		6.52					
		6.31					
		6.69					
	Aliquot 3			6.45	5.32[b]		
				5.2[a]			
				6.44			
				6.39			
	Aliquot 4			6.45			
				5.7[a]			
				6.78			
				6.79			
				6.32			
				6.02			
	n	16	4	12	3	1	2
	Mean $10^3\delta^{18}O_{VSMOW}$ values ± 1s						
	For each laboratory	6.58 ± 0.20	6.88 ± 0.21	6.47 ± 0.25	5.04 ± 0.26	4.74	5.15 ± 0.22
	For analysis type[c]		6.64 ± 0.22			4.97 ± 0.21	
	For all laboratories[c,d]			5.81 ± 0.93			

Table 7 (continued).
$\delta^{18}O_{VSMOW}$ values determined by GS-IRMS for studied apatite samples

Sample ID	Analysis type	"phosphate" $10^3\delta^{18}O_{VSMOW}$ (Ag$_3$PO$_4$-TC/EA)			"bulk" $10^3\delta^{18}O_{VSMOW}$ (LF)		
	Laboratory	Uni Erlangen	Uni Lyon	Uni Missouri	Uni Cape Town	Uni Göttingen	Uni Lausanne
MGMH#128441A	Aliquot 1	7.96 8.04 8.00	8.20 8.55 8.28	7.72 8.3[a] 7.49 7.14	7.63	7.08	7.27
	Aliquot 2	7.89 7.90 7.80		7.42 7.75 8.11	7.42		6.99
	aliquot 3			7.32 7.71 8.01 6.9[a]			7.10
	Aliquot 4			7.92 7.83 7.71 7.59			
	Aliquot 5			7.34 7.44 7.36 7.80 7.51 7.91 7.47 7.30			
	n	6	3	21	2	1	2
	Mean $10^3\delta^{18}O_{VSMOW}$ values $\pm$ 1s						
	For each laboratory	7.93 $\pm$ 0.09	8.34 $\pm$ 0.18	7.61 $\pm$ 0.26	7.53 $\pm$ 0.15	7.08	7.12 $\pm$ 0.14
	For analysis type[c]	7.96 $\pm$ 0.37			7.24 $\pm$ 0.25		
	For all laboratories[c,d]	7.60 $\pm$ 0.48					
MZ-TH	Aliquot 1	10.23 10.43 10.24	10.38 10.44 10.44 10.46 10.09	10.61 9.98 9.78 9.97 11.1[a]	9.30	8.75	10.24
	Aliquot 2	10.54 10.26 10.57		9.94 10.35 9.54	9.91		9.99
	Aliquot 3			9.92 10.36 9.88 9.76	8.75[b]		
	Aliquot 4			10.06 9.71 10.24 9.88	9.36[b]		
	n	6	5	15	4	1	2
	Mean $10^3\delta^{18}O_{VSMOW}$ values $\pm$ 1s						
	For each laboratory	10.38 $\pm$ 0.16	10.36 $\pm$ 0.15	10.00 $\pm$ 0.28	9.33 $\pm$ 0.47	8.75	10.11 $\pm$ 0.18
	For analysis type[c]	10.25 $\pm$ 0.21			9.40 $\pm$ 0.68		
	For all laboratories[c,d]	9.82 $\pm$ 0.65					

Table 7 (continued).
$\delta^{18}O_{VSMOW}$ values determined by GS-IRMS for studied apatite samples

Sample ID	Analysis type	"phosphate" $10^3\delta^{18}O_{VSMOW}$ (Ag$_3$PO$_4$-TC/EA)			"bulk" $10^3\delta^{18}O_{VSMOW}$ (LF)		
	Laboratory	Uni Erlangen	Uni Lyon	Uni Missouri	Uni Cape Town	Uni Göttingen	Uni Lausanne
ES-MM	Aliquot 1	21.87 21.40 21.32 21.66	21.23 21.45 21.51 21.51 21.62	22.54 22.49 22.39 22.28 22.34	21.52	21.23	22.57
	Aliquot 2	21.53 21.35 21.84		22.60 21.96 22.18	20.75		22.40
	Aliquot 3			22.70 22.59 22.14 21.5[a]	20.20		
	Aliquot 4			22.49 22.70 21.90 22.16 22.39	22.20[b]		
	n	7	5	16	4	1	2
	Mean $10^3\delta^{18}O_{VSMOW}$ values $\pm$ 1*s*						
	For each laboratory	21.57 $\pm$ 0.23	21.46 $\pm$ 0.14	22.37 $\pm$ 0.25	21.17 $\pm$ 0.88	21.23	22.48 $\pm$ 0.12
	For analysis type[c]	21.80 $\pm$ 0.49			21.63 $\pm$ 0.74		
	For all laboratories[c,d]	21.71 $\pm$ 0.57					

[a] Outlier values flagged at Uni Missouri were excluded from plots and further interpretation.

[b] Analyses conducted at Uni Cape Town using modified protocol (ClF$_3$ instead of BrF$_5$ as the fluorinating reagent); other analyses employed BrF$_5$. For details see relevant information in "Analytical methods" section.

[c] Uncertainties for an analysis type and all laboratories were calculated based on mean values determined for each laboratory, e.g., 1*s* of $\pm$ 0.22 for MGMH#133648 was calculated based on three mean values for each Ag$_3$PO$_4$-TC/EA laboratory (6.58, 6.88, 6.47).

[d] Current working value for the material.

removing CO_2^{3-} and OH^- from the apatite structure, and therefore, these two components probably had little to no effect on LF determinations. The results of this additional test are consistent with the data collected for other studied samples, showing that a trend of lower, LF-determined $10^3\delta^{18}O$ values (compared with those obtained using Ag$_3$PO$_4$-TC/EA) is applicable to a wide range of phosphate materials, including inorganic apatite (as a separate mineral), phosphate rock such as SARM 32, and biogenic apatite such as tooth enamel (Figure 8).

$\delta^{17}O$ measurements by GS-IRMS

$\delta^{17}O$ data were collected in one GS-IRMS laboratory (at Uni. Göttingen) that has a long-term experience in conducting this type of measurements using laser fluorination (e.g., Gehler *et al.* 2011, Pack and Herwartz 2014, Miller *et al.* 2020). Preliminary $\delta^{17}O$ and $\Delta'^{17}O$ data include a single result for each of the studied apatite samples and the

phosphate rock SARM 32 (Table 8). We should note that further work on these materials is needed in order to assess laboratory bias and uncertainty of $\delta^{17}O$ measurements in apatite. Hence, our ^{17}O data should be seen as only the first step towards a fully satisfactory calibration for triple oxygen isotope determinations in apatite.

SIMS matrix effect and IMF

Instrumental mass fractionation occurring during SIMS measurements of oxygen isotope ratios in minerals and glasses has previously been studied in detail by Eiler *et al.* (1997) who demonstrated that IMF cannot only depend upon sample chemistry (e.g., silicate vs. phosphate), but it may also be influenced by the abundance of certain elements in the mineral structure. A linear mass fraction dependency of IMF during SIMS chlorine isotope ratio analyses has also been reported by the earlier study of the apatite reference materials (Wudarska *et al.* 2021). Based
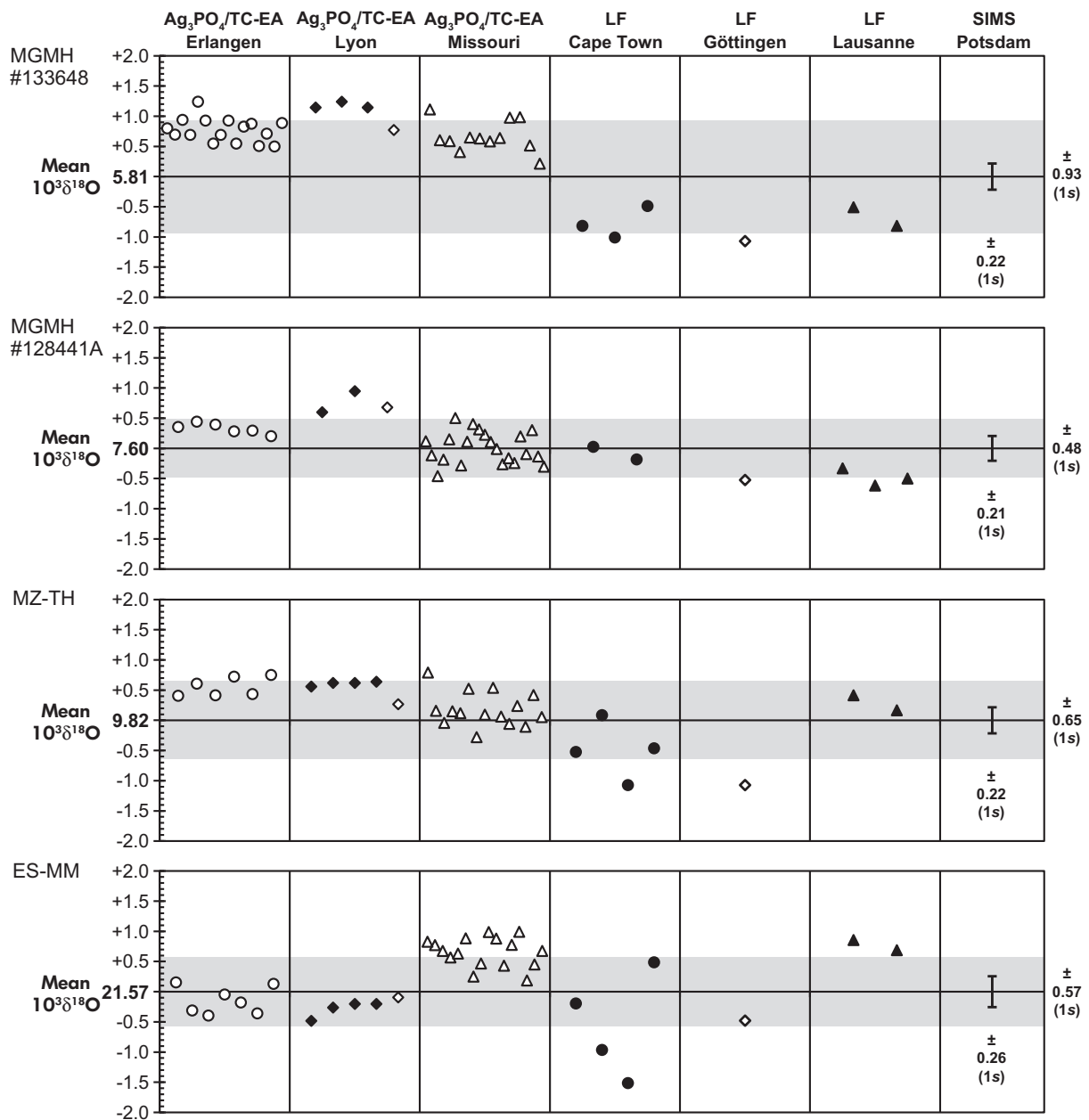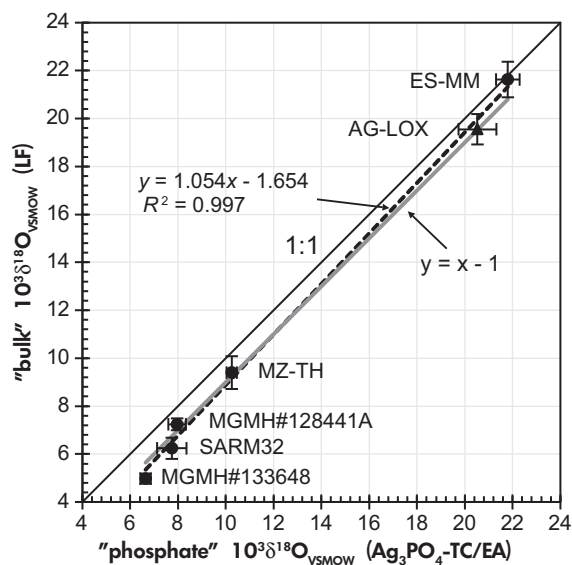
Figure 7. $10^3\delta^{18}O_{VSMOW}$ **values determined independently in six GS-IRMS laboratories in four apatite samples. The** *y*-**axis scale represents the difference between individual analyses and the mean** $10^3\delta^{18}O_{VSMOW}$ **values, while the grey areas represent** 1*s* **(Table 7). The vertical bar in the SIMS column represents total uncertainty of the SIMS measurements (** $\pm$ **1***s*, **uncertainties of individual analyses and repeatability during homogeneity testing of Mount #3, Table 6).**

on $10^3\delta^{18}O_{VSMOW}$ values determined in six GS-IRMS laboratories (Table 7), we do not observe any correlation between SIMS α_{inst} and chemical characteristics of the studied apatite samples, for example, mole fractions of Ca+P (X_{Ca+P}, see subsection "Chemical compositions") that could be distinguished from the relatively large

data spreads derived from GS-IRMS measurements (Figure 9).

Taking into consideration non-systematic variations between the GS-IRMS datasets that do not correspond to the phosphate-bonded and "bulk" oxygen contents
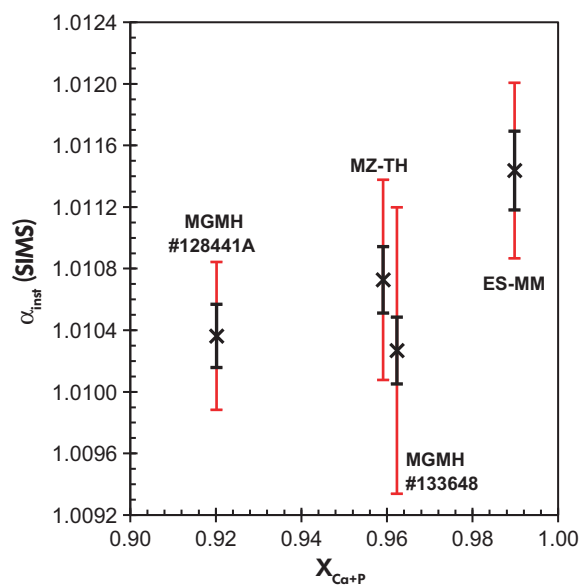
Figure 8. Comparison of mean $10^3\delta^{18}O_{VSMOW}$ values determined for the four studied apatite samples (Table 7), SARM 32 (Table S5.2 in Appendix S5), and AG-LOX (Tables S7.1 and S7.2 in Appendix S7) obtained from reaction of Ag_3PO_4 with graphite in a continuous flow TC-EA ("phosphate" $\delta^{18}O$) with those obtained by laser fluorination ("bulk" $\delta^{18}O$). The black dashed line represents a best-fit regression line for all data points, while the grey one corresponds to a regression line with a slope of 1.0 that is displaced by 1.0. The horizontal and vertical bars represent 1s.

Figure 9. α_{inst} in SIMS determined for the four apatite samples vs. mole fractions of Ca+P calculated based on EPMA data (Table 3 and 4) and calibrated with the mean $10^3\delta^{18}O_{VSMOW}$ values reported in Tables 7 and 9. The black bars represent total uncertainty of the SIMS measurements ($\pm$ 1s, uncertainty of individual analyses and repeatability during homogeneity testing of Mount #3, Table 6). The red bars represent $\pm$ 1s of $10^3\delta^{18}O_{VSMOW}$ determinations in six GS-IRMS laboratories (Table 7).

Table 8.
Preliminary ^{17}O data for the studied apatite samples and the phosphate rock SARM 32

Sample ID	"bulk" $10^3\delta^{17}O_{VSMOW}$	"bulk" $\Delta'^{17}O_{0.528}$ (ppm)
MGMH#133648	2.44	-58
MGMH#128441A	3.67	-59
MZ-TH	4.53	-79
ES-MM	11.06	-93
SARM 32	3.07	-60

estimated based on EPMA, TG, and IR, the current working values for SIMS data calibration are based on six equally weighted mean values determined in all six GS-IRMS laboratories. SIMS-determined $10^3\delta^{18}O_{VSMOW}$ values for MGMH#133648, MGMH#128441A, and MZ-TH, which were calculated assuming that one of the samples acted as a reference material, while the others were unknowns, correspond well with the mean GS-IRMS values (Table 9). In

contrast, the SIMS result for ES-MM indicates that this sample is characterised by a significantly higher $10^3\delta^{18}O_{VSMOW}$ value than the mean value defined by GS-IRMS. The reason for this discrepancy is unknown; therefore, this material might, at the current time, more appropriately serve as a quality control material for monitoring instrumental stability.

Conclusions

Metrological splits of the apatite samples described here can be obtained through the IAGeo Limited website (www. iageo.com). Determined $10^3\delta^{18}O_{VSMOW}$ values are method-specific, and therefore, the recommended $10^3\delta^{18}O_{VSMOW}$ working values and preliminary ^{17}O data shown in Table 10 are subject to future revision as data generated by differing sample preparation, and measurement strategies become harmonised. Three reference materials – MGMH#133648, MGMH#128441A, and MZ-TH – are suitable for calibration of the *in situ* $\delta^{18}O$ measurements, while ES-MM might at the current time more appropriately serves as a quality control material (e.g., for

Table 9.
$10^3\delta^{18}O_{VSMOW}$ values for the studied apatite samples determined by SIMS

Mean $10^3\delta^{18}O_{VSMOW} \pm 1s$ (GS-IRMS)[a]		$10^3\delta^{18}O_{VSMOW}$ (SIMS)[b]			
		MGMH#133648	MGMH#128441A	MZ-TH	ES-MM
MGMH#133648	5.81 ± 0.93	–	7.69	10.28	22.89
MGMH#128441A	7.60 ± 0.48	5.72	–	10.18	22.80
MZ-TH	9.82 ± 0.65	5.35	7.24	–	22.43
ES-MM	21.71 ± 0.57	4.65	6.53	9.11	–

[a] $10^3\delta^{18}O_{VSMOW}$ data calculated based on equally weighted mean values determined in six GS-IRMS laboratories and uncertainty based on the standard deviation of the six values.
[b] The SIMS data in each row was calculated based on α_{inst} obtained during homogeneity tests of Mount #3 (Figure 9), assuming that one of the samples acted as a reference material, while the other three were treated as unknowns.

Table 10.
Summary of current working values for the four studied apatite samples

Sample ID	$10^3\delta^{18}O_{VSMOW}$ (± 1s)			$10^3\delta^{17}O_{VSMOW}$	$\Delta'^{17}O_{0.528}$ (ppm)
	Ag_3PO_4-TC/EA	Laser fluorination	SIMS[a]	Laser fluorination[b]	
MGMH#133648	6.64 ± 0.22	4.97 ± 0.21	5.81 ± 0.93	2.44	-58
MGMH#128441A	7.96 ± 0.37	7.24 ± 0.25	7.60 ± 0.48	3.67	-59
MZ-TH	10.25 ± 0.21	9.40 ± 0.68	9.82 ± 0.65	4.53	-79
ES-MM	21.80 ± 0.49	21.63 ± 0.74	21.71 ± 0.57	11.06	-93

[a] $10^3\delta^{18}O_{VSMOW}$ data calculated based on equally weighted mean values determined in six GS-IRMS laboratories and uncertainty based on the standard deviation of the six values.
[b] $10^3\delta^{17}O_{VSMOW}$ and $\Delta'^{17}O$ values determined using laser fluorination (preliminary data collected in only one laboratory).

monitoring instrumental stability). We advise collecting BSE and reflected-light optical images of mounted polished crystals prior to SIMS isotope work in order to avoid any possible inclusions; this is of special importance for the chlorapatite MGMH#133648 that may contain traces of OH-enriched domains. Due to the offset between $10^3\delta^{18}O_{VSMOW}$ values determined by GS-IRMS, our recommendation for future SIMS-based studies of minerals from the apatite group is to use at least two reference materials. Furthermore, when interpreting SIMS data, we recommend taking into account that the total uncertainty of SIMS measurements based on our RMs would be at the level of ± ~ 0.5, despite better capabilities offered by large geometry instruments.

Acknowledgements

Data availability statement

The data that support the findings of this study are available in the Supplementary Material and from the corresponding author upon request.

References

Baertschi P. (1976)
Absolute ^{18}O content of standard mean ocean water. Earth and Planetary Science Letters, 31, 341–344.

Bellucci J.J., Whitehouse M.J., Nemchin A.A., Snape J.F., Kenny G.G., Merle R.E., Bland P.A. and Benedix G.K. (2020)
Tracing martian surface interactions with the triple O isotope compositions of meteoritic phosphates. Earth and Planetary Science Letters, 531, 115977.

Blake R.E., Chang S.J. and Lepland A. (2010)
Phosphate oxygen isotopic evidence for a temperate and biologically active Archaean ocean. Nature, 464, 1029–1032.

Brand W.A., Coplen T.B., Vogl J., Rosner M. and Prohaska T. (2014)
Assessment of international reference materials for isotope-ratio analysis (IUPAC Technical Report). Pure and Applied Chemistry, 86, 425–467.

Bruand E., Storey C., Fowler M., Heilimo E. and EIMF (2019)
Oxygen isotopes in titanite and apatite, and their potential for crustal evolution research. Geochimica et Cosmochimica Acta, 255, 144–162.

Bryant J.D., Koch P.L., Froelich P.N., Showers W.J. and Genna B.J. (1996)
Oxygen isotope partitioning between phosphate and carbonate in mammalian apatite. Geochimica et Cosmochimica Acta, 60, 5145–5148.

Chen J., Shen S.Z., Li X.H., Xu Y.G., Joachimski M.M., Bowring S.A., Erwin D.H., Yuan D.X., Chen B., Zhang H., Wang Y., Cao C.Q., Zheng Q.F. and Mu L. (2016)
High-resolution SIMS oxygen isotope analysis on conodont apatite from South China and implications for the end-Permian mass extinction. Palaeogeography, Palaeoclimatology, Palaeoecology, 448, 26–38.

Chen J., Shen S.Z., Zhang Y.C., Angiolini L., Gorgij M.N., Crippa G., Wang W., Zhang H., Yuan D.X., Li X.H. and Xu Y.G. (2020)
Abrupt warming in the latest Permian detected using high-resolution in situ oxygen isotopes of conodont apatite from Abadeh, central Iran. Palaeogeography, Palaeoclimatology, Palaeoecology, 560, 109973.

Chickerur N.S., Tung M.S. and Brown W.E. (1980)
A mechanism for incorporation of carbonate into apatite. Calcified Tissue International, 32, 55–62.

Coplen T.B. (2011)
Guidelines and recommended terms for expression of stable-isotope-ratio and gas-ratio measurement results. Rapid Communications in Mass Spectrometry, 25, 2538–2560.

Coplen T.B., Kendall C. and Hopple J. (1983)
Comparison of stable isotope reference samples. Nature, 302, 236–238.

Crowson R.A., Showers W.J., Wright E.K. and Hoering T.C. (1991)
Preparation of phosphate samples for oxygen isotope analysis. Analytical Chemistry, 63, 2397–2400.

Decrée S., Cawthorn G., Deloule E., Mercadier J., Frimmel H. and Baele J.-M. (2020)
Unravelling the processes controlling apatite formation in the Phalaborwa Complex (South Africa) based on combined cathodoluminescence, LA-ICPMS and in-situ O and Sr isotope analyses. Contributions to Mineralogy and Petrology, 175, 1–31.

Edwards C.T., Jones C.M., Quinton P.C. and Fike D.A. (2022)
Oxygen isotope ($\delta^{18}O$) trends measured from Ordovician conodont apatite using secondary ion mass spectrometry (SIMS): Implications for paleo-thermometry studies. Geological Society of America Bulletin, 134, 261–274.

Eiler J.M., Graham C. and Valley J.W. (1997)
SIMS analysis of oxygen isotopes: matrix effects in complex minerals and glasses. Chemical Geology, 138, 221–244.

Elliott J.C. (1994)
Structure and chemistry of the apatites and other calcium orthophosphates. Elsevier (Amsterdam), 389pp.

Gehler A., Tütken T. and Pack A. (2011)
Triple oxygen isotope analysis of bioapatite as tracer for diagenetic alteration of bones and teeth. Palaeogeography, Palaeoclimatology, Palaeoecology, 310, 84–91.

Gehler A., Tütken T. and Pack A. (2012)
Oxygen and carbon isotope variations in a modern rodent community – Implications for palaeoenvironmental reconstructions. PLoS One, 7, e49531.

Goldoff B., Webster J.D. and Harlov D.E. (2012)
Characterization of fluor-chlorapatites by electron probe microanalysis with a focus on time-dependent intensity variation of halogens. American Mineralogist, 97, 1103–1115.

Gonfiantini R., Stichler W. and Rozanski K. (1995)
Standards and intercomparison materials distributed by the International Atomic Energy Agency for stable isotope measurements. In: Reference and intercomparison materials for stable isotopes of light elements. No. IAEA-TECDOC-825. International Atomic Energy Agency (Vienna), 13–29.

Gonfiantini R., Tonarini S., Gröning M., Adorni-Braccesi A., Al-Ammar A.S., Astner M., Bächler S., Barnes R.M., Bassett R.L., Cocherie A., Deyhle A., Dini A., Ferrara G., Gaillardet J., Grimm J., Guerrot C., Krähenbühl U., Layne G., Lemarchand D., Meixner A., Northington D.J., Pennisi M., Reitznerová E., Rodushkin I., Sugiura N., Surberg R., Tonn S., Wiedenbeck M., Wunderli S., Xiao Y. and Zack T. (2003)
Intercomparison of boron isotope and concentration measurements. Part II: Evaluation of results. Geostandards Newsletter: The Journal of Geostandards and Geoanalysis, 27, 41–57.

Greenwood J.P., Blake R.E. and Coath C.D. (2003)
Ion microprobe measurements of $^{18}O/^{16}O$ ratios of phosphate minerals in the Martian meteorites ALH84001 and Los Angeles. Geochimica et Cosmochimica Acta, 67, 2289–2298.

references

Hansen R.G. (1985)
The preparation and certification of a South African phosphate concentrate for use as a reference material. Report No. M190. Council for Mineral Technology (Randburg), 19pp.

Harris C. and Vogeli J. (2010)
Oxygen isotope composition of garnet in the Peninsula Granite, Cape Granite Suite, South Africa: Constraints on melting and emplacement mechanisms. South African Journal of Geology, 113, 401–412.

Huberty J.M., Kita N.T., Kozdon R., Heck P.R., Fournelle J.H., Spicuzza M.J., Xu H. and Valley J.W. (2010)
Crystal orientation effects in $\delta^{18}O$ for magnetite and hematite by SIMS. Chemical Geology, 276, 269–283.

Jaisi D.P. and Blake R.E. (2014)
Advances in using oxygen isotope ratios of phosphate to understand phosphorus cycling in the environment. Advances in Agronomy, 125, 1–53.

Joachimski M.M., Breisig S., Buggisch W., Talent J.A., Mawson R., Gereke M., Morrow J.R., Day J. and Weddige K. (2009)
Devonian climate and reef evolution: Insights from oxygen isotopes in apatite. Earth and Planetary Science Letters, 284, 599–609.

Ketcham R.A. (2015)
Calculation of stoichiometry from EMP data for apatite and other phases with mixing on monovalent anion sites. American Mineralogist, 100, 1620–1623.

Kita N.T., Huberty J.M., Kozdon R., Beard B.L. and Valley J.W. (2011)
High-precision SIMS oxygen, sulfur and iron stable isotope analyses of geological materials: Accuracy, surface topography and crystal orientation. Surface and Interface Analysis, 43, 427–431.

Kohn M.J. and Cerling T.E. (2002)
Stable isotope compositions of biological apatite. Reviews in Mineralogy and Geochemistry, 48, 455–488.

Kohn M.J., Schoeninger M.J. and Barker W.W. (1999)
Altered states: Effects of diagenesis on fossil tooth chemistry. Geochimica et Cosmochimica Acta, 63, 2737–2747.

Kolodny Y., Luz B. and Navon O. (1983)
Oxygen isotope variations in phosphate of biogenic apatites, I. Fish bone apatite – Rechecking the rules of the game. Earth and Planetary Science Letters, 64, 398–404.

Kwaśniak-Kominek M., Manecki M., Matusik J. and Lempart M. (2017)
Carbonate substitution in lead hydroxyapatite $Pb_5(PO_4)_3OH$. Journal of Molecular Structure, 1147, 594–602.

Lécuyer C. (2004)
Oxygen isotope analysis of phosphate. In: de Grot P.A. (ed.), Handbook of stable isotope analytical techniques. Elsevier (Amsterdam), 482–496.

Lécuyer C., Fourel F., Seris M., Amiot R., Goedert J. and Simon L. (2019)
Synthesis of in-house produced calibrated silver phosphate with a large range of oxygen isotope compositions. Geostandards and Geoanalytical Research, 43, 681–688.

Lécuyer C., Grandjean P., O'Neil J.R., Cappetta H. and Martineau F. (1993)
Thermal excursions in the ocean at the Cretaceous-Tertiary boundary (northern Morocco): $\delta^{18}O$ record of phosphatic fish debris. Palaeogeography, Palaeoclimatology, Palaeoecology, 105, 235–243.

Lempart M., Manecki M., Kwaśniak-Kominek M., Matusik J. and Bajda T. (2019)
Accommodation of the carbonate ion in lead hydroxyl arsenate (hydroxylmimetite) $Pb_5(AsO_4)_3OH$. Polyhedron, 161, 330–337.

Leventouri T., Chakoumakos B.C., Moghaddam H.Y. and Perdikatsis V. (2000)
Powder neutron diffraction studies of a carbonate fluorapatite. Journal of Materials Research, 15, 511–517.

Li W., Ni B., Jin D. and Zhang Q. (1988)
Measurement of the absolute abundance of oxygen-17 in V-SMOW. Kexue Tongbao, 33, 1610–1613.

Li Y., Tang G.Q., Liu Y., He S., Chen B., Li Q.L and Li X.H. (2021)
Revisiting apatite SIMS oxygen isotope analysis and Qinghu-AP reference material. Chemical Geology, 582, 120445.

Longinelli A. (1965)
Oxygen isotopic composition of orthophosphate from shells of living marine organisms. Nature, 207, 716–719.

Longinelli A. (1984)
Oxygen isotopes in mammal bone phosphate: A new tool for paleohydrological and paleoclimatological research. Geochimica et Cosmochimica Acta, 48, 385–390.

Luz B. and Kolodny Y. (1985)
Oxygen isotope variations in phosphate of biogenic apatites, IV. Mammal teeth and bones. Earth and Planetary Science Letters, 75, 29–36.

Luz B., Kolodny Y. and Kovach J. (1984)
Oxygen isotope variations in phosphate of biogenic apatites, III. Conodonts. Earth and Planetary Science Letters, 69, 255–262.

MacLeod K.G. (2012)
Conodonts and the paleoclimatological and paleoecological applications of phosphate $\delta^{18}O$ measurements. The Paleontological Society Papers, 18, 69–84.

references

Manzini M., Bouvier A.-S., Barnes J.D., Bonifacie M., Rose-Koga E.F., Ulmer P., Métrich N., Bardoux G., Williams J., Layne G.D., Straub S., Baumgartner L.P. and John T. (2017)
SIMS chlorine isotope analyses in melt inclusions from arc settings. Chemical Geology, 449, 112–122.

McLaughlin K., Kendall C., Silva S.R., Young M. and Paytan A. (2006)
Phosphate oxygen isotope ratios as a tracer for sources and cycling of phosphate in North San Francisco Bay, California. Journal of Geophysical Research: Biogeosciences, 111, G03003.

Meisel T.C. (2019)
Why δ is not ‰ and why we should not use ε and μ notations. Geostandards and Geoanalytical Research, 43, 527–528.

Miller M.F. and Pack A. (2021)
Why measure ^{17}O? Historical perspective, triple-isotope systematics and selected applications. Reviews in Mineralogy and Geochemistry, 86, 1–34.

Miller M.F., Pack A., Bindeman I.N. and Greenwood R.C. (2020)
Standardizing the reporting of $\Delta^{17}O$ data from high precision oxygen triple-isotope ratio measurements of silicate rocks and minerals. Chemical Geology, 532, 119332.

O'Neil J.R., Roe L.J., Reinhard E. and Blake R.E. (1994)
A rapid and precise method of oxygen isotope analysis of biogenic phosphate. Israel Journal of Earth Sciences, 43, 203–212.

Pack A. and Herwartz D. (2014)
The triple oxygen isotope composition of the Earth mantle and understanding $\Delta^{17}O$ variations in terrestrial rocks and minerals. Earth and Planetary Science Letters, 390, 138–145.

Pack A., Tanaka R., Hering M., Sengupta S., Peters S. and Nakamura E. (2016)
The oxygen isotope composition of San Carlos olivine on the VSMOW2-SLAP2 scale. Rapid Communications in Mass Spectrometry, 30, 1495–1504.

Pan Y. and Fleet M.E. (2002)
Compositions of the apatite-group minerals: Substitution mechanisms and controlling factors. Reviews in Mineralogy and Geochemistry, 48, 13–49.

Passey B.H. and Levin N.E. (2021)
Triple oxygen isotopes in meteoric waters, carbonates, and biological apatites: Implications for continental paleoclimate reconstruction. Reviews in Mineralogy and Geochemistry, 86, 429–462.

Paul D., Skrzypek G. and Fórizs I. (2007)
Normalization of measured stable isotopic compositions to isotope reference scales – A review. Rapid Communications in Mass Spectrometry, 21, 3006–3014.

Pederzani S., Snoeck C., Wacker U. and Britton K. (2020)
Anion exchange resin and slow precipitation preclude the need for pretreatments in silver phosphate. Chemical Geology, 534, 119455.

Pucéat E., Joachimski M.M., Bouilloux A., Monna F., Bonin A., Motreuil S., Morinière P., Hénard S., Mourin J., Dera G. and Quesne D. (2010)
Revised phosphate-water fractionation equation reassessing paleotemperatures derived from biogenic apatite. Earth and Planetary Science Letters, 298, 135–142.

Quinton P.C. and MacLeod K.G. (2014)
Oxygen isotopes from conodont apatite of the midcontinent, US: Implications for Late Ordovician climate evolution. Palaeogeography, Palaeoclimatology, Palaeoecology, 404, 57–66.

Regnier P., Lasaga A.C. and Berner R.A. (1994)
Mechanism of CO_3^{2-} substitution in carbonate-fluorapatite: Evidence from FTIR spectroscopy, ^{13}C NMR, and quantum mechanical calculations. American Mineralogist, 79, 809–818.

Santos R.V. and Clayton R.N. (1995)
The carbonate content in high-temperature apatite: An analytical method applied to apatite from the Jacupiranga alkaline complex. American Mineralogist, 80, 336–344.

Schoenemann S.W., Schauer A.J. and Steig E.J. (2013)
Measurement of SLAP2 and GISP $\delta^{17}O$ and proposed VSMOW-SLAP normalization for $\delta^{17}O$ and $^{17}O_{excess}$. Rapid Communications in Mass Spectrometry, 27, 582–590.

Seitz S., Baumgartner L.P., Bouvier A.-S., Putlitz B. and Vennemann T. (2017)
Quartz reference materials for oxygen isotope analysis by SIMS. Geostandards and Geoanalytical Research, 41, 69–75.

Sharp Z.D., Gibbons J.A., Maltsev O., Atudorei V., Pack A., Sengupta S., Shock E.L. and Knauth L.P. (2016)
A calibration of the triple oxygen isotope fractionation in the SiO_2–H_2O system and applications to natural samples. Geochimica et Cosmochimica Acta, 186, 105–119.

Sharp Z.D., Wostbrock J.A.G. and Pack A. (2018)
Mass-dependent triple oxygen isotope variations in terrestrial materials. Geochemical Perspectives Letters, 7, 27–31.

Shemesh A., Kolodny Y. and Luz B. (1983)
Oxygen isotope variations in phosphate of biogenic apatites, II. Phosphorite rocks. Earth and Planetary Science Letters, 64, 405–416.

Shemesh A., Kolodny Y. and Luz B. (1988)
Isotope geochemistry of oxygen and carbon in phosphate and carbonate of phosphorite francolite. Geochimica et Cosmochimica Acta, 52, 2565–2572.

Stormer J.C., Pierson M.L. and Tacker R.C. (1993)
Variation of F and Cl X-ray intensity due to anisotropic diffusion in apatite during electron microprobe analysis. American Mineralogist, 78, 641–648.

references

Sun Y., Wiedenbeck M., Joachimski M.M., Beier C., Kemner F. and Weinzierl C. (2016)
Chemical and oxygen isotope composition of gem-quality apatites: Implications for oxygen isotope reference materials for secondary ion mass spectrometry (SIMS). Chemical Geology, 440, 164–178.

Tacker R.C. (2008)
Carbonate in igneous and metamorphic fluorapatite: Two type A and two type B substitutions. American Mineralogist, 93, 168–176.

Tõnsuaadu K., Gross K.A., Plūduma L. and Veiderma M. (2012)
A review on the thermal stability of calcium apatites. Journal of Thermal Analysis and Calorimetry, 110, 647–659.

Tõnsuaadu K., Peld M. and Bender V. (2003)
Thermal analysis of apatite structure. Journal of Thermal Analysis and Calorimetry, 72, 363–371.

Trotter J.A., Williams I.S., Barnes C.R., Lécuyer C. and Nicoll R.S. (2008)
Did cooling oceans trigger Ordovician biodiversification? Evidence from conodont thermometry. Science, 321, 550–554.

Trotter J.A., Williams I.S., Nicora A., Mazza M. and Rigo M. (2015)
Long-term cycles of Triassic climate change: A new $\delta^{18}O$ record from conodont apatite. Earth and Planetary Science Letters, 415, 165–174.

Urey H.C., Lowenstam H.A., Epstein S. and McKinney C.R. (1951)
Measurement of paleotemperatures and temperatures of the Upper Cretaceous of England, Denmark, and the southeastern United States. Geological Society of America Bulletin, 62, 399–416.

Valley J.W., Kitchen N., Kohn M.J., Niendorf C.R. and Spicuzza M.J. (1995)
UWG-2, a garnet standard for oxygen isotope ratios: Strategies for high precision and accuracy with laser heating. Geochimica et Cosmochimica Acta, 59, 5223–5231.

Vennemann T.W., Fricke H.C., Blake R.E., O'Neil J.R. and Colman A. (2002)
Oxygen isotope analysis of phosphates: a comparison of techniques for analysis of Ag_3PO_4. Chemical Geology, 185, 321–336.

Vennemann T.W., Morlok A., von Engelhardt W. and Kyser K. (2001)
Stable isotope composition of impact glasses from the Nördlinger Ries impact crater, Germany. Geochimica et Cosmochimica Acta, 65, 1325–1336.

Wheeley J.R., Smith M.P. and Boomer I. (2012)
Oxygen isotope variability in conodonts: Implications for reconstructing Palaeozoic palaeoclimates and palaeoceanography. Journal of the Geological Society of London, 169, 239–250.

Wiedenbeck M., Trumbull R.B., Rosner M., Boyce A., Fournelle J.H., Franchi I.A., Halama R., Harris C., Lacey J.H., Marschall H., Meixner A., Pack A., Pogge von Strandmann P.A., Spicuzza M.J., Valley J.W. and Wilke F.D. (2021)
Tourmaline reference materials for the in situ analysis of oxygen and lithium isotope ratio compositions. Geostandards and Geoanalytical Research, 45, 97–119.

Wostbrock J.A.G., Cano E.J. and Sharp Z.D. (2020)
An internally consistent triple oxygen isotope calibration of standards for silicates, carbonates and air relative to VSMOW2 and SLAP2. Chemical Geology, 533, 119432.

Wu L., Shi G., Danišík M., Zhang Z., Wang Y. and Wang F. (2019)
MK-1 apatite: A new potential reference material for (U-Th)/He dating. Geostandards and Geoanalytical Research, 43, 301–315.

Wudarska A., Słaby E., Wiedenbeck M., Barnes J.D., Bonifacie M., Sturchio N.C., Bardoux G., Couffignal F., Glodny J., Linnea H., John T., Kusebauch C., Mayanna S., Wilke F.D.H. and Deput E. (2021)
Inter-laboratory characterisation of apatite reference materials for chlorine isotope analysis. Geostandards and Geoanalytical Research, 45, 121–142.

Xu W.G., Fan H.R., Hu F.F., Santosh M., Yang K.F. and Lan T.G. (2015)
In situ chemical and Sr–Nd–O isotopic compositions of apatite from the Tongshi intrusive complex in the southern part of the North China Craton: Implications for petrogenesis and metallogeny. Journal of Asian Earth Sciences, 105, 208–222.

Xu Z., Huang T. and Yin X. (2018)
Improvements in the preparation of phosphate for oxygen isotope analysis from soils and sediments. PLoS One, 13, e0204203.

Yang Q., Xia X.-P., Zhang L., Zhang W., Zhang Y., Chen L., Yang Y. and He M. (2020)
Oxygen isotope homogeneity assessment for apatite U-Th-Pb geochronology reference materials. Surface and Interface Analysis, 52, 197–213.

Young E.J. and Munson E.L. (1966)
Fluor-chlor-oxy-apatite and sphene from crystal lode pegmatite near Eagle, Colorado. American Mineralogist, 51, 1476–1493.

Zeng L.P., Zhao X.F., Li X.C., Hu H. and McFarlane C. (2016)
In situ elemental and isotopic analysis of fluorapatite from the Taocun magnetite-apatite deposit, Eastern China: Constraints on fluid metasomatism. American Mineralogist, 101, 2468–2483.

references

Zhang X., Guo F., Zhang B., Zhao L. and Wang G. (2021)
Mixing of cogenetic magmas in the Cretaceous Zhangzhou calc-alkaline granite from southeast China recorded by *in-situ* apatite geochemistry. **American Mineralogist**, 106, 1679–1689.

Žigaitė Ž. and Whitehouse M. (2014)
Stable oxygen isotopes of dental biomineral: Differentiation at the intra- and inter-tissue level of modern shark teeth. GFF, 136, 337–340.

Supporting information

The following supporting information may be found in the online version of this article:

Appendix S1. Description and the datasets collected for an additional sample TUBAF#43.

Appendix S2. Reflected-light optical microscope and back-scattered electron images of Mount#4 (MGMH#133648 chlorapatite).

Appendix S3. Reflected-light optical microscope image of Mount#5 (Dur fluorapatite).

Appendix S4. Topographic model and dimensions of a typical SIMS crater.

Appendix S5. Oxygen isotope composition of the phosphate rock SARM 32.

Appendix S6. Yields of the oxygen isotope measurements by laser fluorination.

Appendix S7. GS-IRMS dataset for AG-LOX (tooth enamel of a modern African elephant).

Appendix S8. Complete EPMA data tables (5 nA and 40 nA).

Appendix S9. Further information on the substitution of CO_3^{2-} and OH^- in the apatite samples.

Appendix S10. Complete SIMS data tables.

This material is available from: http://onlinelibrary.wiley.com/doi/10.1111/ggr.12416/abstract (This link will take you to the article abstract).